Frequency-dependent seismic radiation process of the 2024 Noto Peninsula earthquake from teleseismic P-wave back-projection

K. Tarumi[1,*] and K. Yoshizawa[1,2]

[1] Department of Natural History Sciences, Graduate School of Science, Hokkaido University, Sapporo 060-0810, Japan

[2]Department of Earth & Planetary Sciences, Faculty of Science, Hokkaido University, Sapporo 060-0810, Japan.

[*]Corresponding author: tarumi.kotaro.jp@gmail.com

This is a revised preprint submitted to EarthArXiv. The revised manuscript has been resubmitted to *Earth and Planetary Science Letters* following peer review.

Highlights

Frequency-dependent seismic radiation process of the 2024 Noto Peninsula earthquake from teleseismic P-wave back-projection

Kotaro Tarumi, Kazunori Yoshizawa

- The source process of the 2024 Noto earthquake is imaged by P-wave back-projection.
- Multi-frequency back-projection images reveal complex fault rupture sequences.
- Main source rupture propagates bilaterally toward inland and offshore regions.
- High-frequency P-waves are radiated before the rapid main rupture propagation.
- Frequency-dependent P-wave radiations reflect the effects of complex fault geometry.

Frequency-dependent seismic radiation process of the 2024 Noto Peninsula earthquake from teleseismic P-wave back-projection

Kotaro Tarumi[a,b], Kazunori Yoshizawa[a,b]

[a]*Department of Natural History Sciences, Graduate School of Science, Hokkaido University, Sapporo 060-0810, Japan., Sapporo, 060-0810, Japan*
[b]*Department of Earth and Planetary Sciences, Faculty of Science, Hokkaido University, Sapporo, 060-0810, Japan*

Abstract

A large devastating earthquake of Mw 7.5 struck the Noto Peninsula, Japan, on January 1st, 2024. Persistent seismic swarms have preceded the main rupture around the hypocenter since 2020, likely driven by crustal fluids migrating upward from the lower crust. In this study, we investigated the frequency-dependent seismic radiation process using multi-frequency teleseismic P-wave back projection. The resulting source process reveals complex frequency-dependent behavior, which can be divided into four episodes. The initial episode lasts 15–20 s, characterized by high-frequency energy preceding low-frequency radiation. The second episode is marked by intense high-frequency P-wave emission with the absence of low-frequency signals. Then, intensive low-frequency P-waves are radiated from the source region, with ruptures propagating bilaterally from the hypocentral area toward the southwestern inland (third episode) and northeastern offshore (fourth episode) regions. The fluid-rich condition near the hypocenter likely plays an important role in controlling fault rupture, contributing to the observed complex rupture processes. The intricate fault geometry around the source region may have also contributed to the characteristic frequency-dependence of P-wave radiation during this earthquake.

Keywords: 2024 Noto Earthquake, P-wave radiation, back projection, source process, crustal fluid, fault geometry

---

1. Introduction

On January 1st, 2024, a large and devastating earthquake with a moment magnitude (Mw) of 7.5 (Global CMT (GCMT):Ekström et al. (2012), Japan Meteorological Agency: JMA (2024b)) occurred in the Noto Peninsula in Japan, causing widespread destruction and collapse of numerous buildings, with over 400 casualties reported by the Fire and Disaster Management Agency (FDMA, 2024) of Japan. Several locations recorded the maximum seismic intensity of 7, the highest on the JMA scale, with the Noto Peninsula experiencing strong ground motion and coastal uplift. This earthquake also generated a tsunami with a maximum height of 5 meters, which was observed not only around the peninsula but also in Korea, North Korea, and Russia (Fujii and Satake, 2024; Mizutani et al., 2024).

This destructive earthquake has been identified as a thrust fault based on local (JMA, 2024a,b) and global seismic waveform analyses (e.g., GCMT) (Figure 1). The aftershock distribution provided by JMA indicates that the source fault length extends to about 150 km (JMA, 2024a) (colored dots in

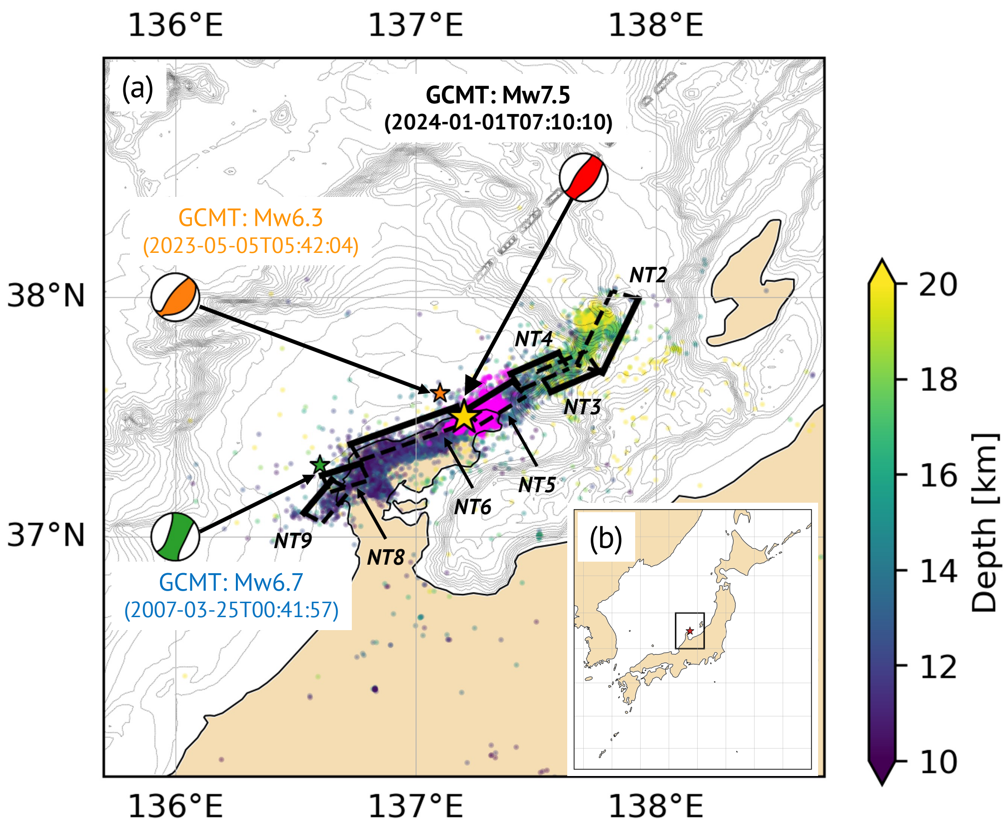

Figure 1: (a) The locations of the Mw 7.5 2024 Noto Peninsula Earthquake on January 1st, 2024, and its aftershocks as well as recent large earthquakes in our study area. All origin times are in UTC. The yellow star and red focal mechanism represent the epicenter of the Mw 7.5 event on January 1st, 2024, and its focal mechanism from Global CMT. Colored dots indicate the distribution of aftershocks until January 14th, 2024 (JMA, 2024a), whose legends are displayed on the right. The other two stars and corresponding focal mechanisms denote past large events in 2007 and 2023. Magenta dots represent the preceding seismic events (since November 2020) leading to the Mw 7.5 mainshock, as reported by Yoshida et al. (2023a). Seven black rectangles exhibit the fault models from the Japan Sea earthquake and tsunami project (JSPJ) (MEXT, 2021), NT2, NT3, NT4, NT5, NT6, NT8, and NT9, in which solid black lines indicate the top of each fault. Inset (b) displays a broader-scale map indicating the location of the study area. The black rectangle encompasses the area shown in (a), where the red star marks the epicenter of the Mw 7.5 main event reported by USGS (USGS, 2024).

Figure 1), which is longer than other inland earthquakes of similar magnitude in Japan. In addition, the fault geometry appears complex; the inland region mainly dips toward the southeast, while the offshore region may involve northwest-dipping faults (Ministry of Education, Culture, Sports, Science and Technology, Japan: MEXT, 2021), according to the comprehensive fault model constructed by seismic and geological surveys. Also, the intricate geometry of source faults can be seen in the automatically determined aftershocks (Figure 1), which has recently been reconfirmed by the precise determination using the ocean-bottom seismometers (Shinohara et al., 2025). Several studies have analyzed the seismic source process using the seismic records from near-field and teleseismic stations, geodetic data (e.g., GNSS), and local tsunami waveforms (e.g., Fujii and Satake, 2024; Okuwaki et al., 2024; Mizutani et al., 2024; Kutschera et al., 2024; Ma et al., 2024; Xu et al., 2024; Liu et al., 2024; Yamada et al., 2025). Many of these studies have identified two large-slip areas in the western inland and eastern offshore regions of the Noto Peninsula, resulting from bilateral rupture propagation from the hypocentral region toward these slip areas.

Seismic swarms have occurred near the hypocenter of the Mw 7.5 event since November 2020 (e.g., Amezawa et al., 2023; Nishimura et al., 2023; Yoshida et al., 2023b), likely driven by the upward migration of fluid (Nishimura et al., 2023). The presence of high pore pressure may be related to the complex fault rupture processes; Marguin and Simpson (2023) numerically modeled the reduction of rupture and slip velocity on fault, while Pampillón et al.

(2023) suggested the fault rupture speed reached the supershear through the rock experiment. Additionally, fluids can effectively weaken the fault cohesion, possibly causing the fault to slip more easily (Madden et al., 2022). Earlier works employing seismic data (Okuwaki et al., 2024; Kutschera et al., 2024; Ma et al., 2024; Xu et al., 2024) suggest that the complex source process within the intricate fault network may be controlled by upward-migrating crustal fluids. Yoshida et al. (2024) relocated the aftershock distribution and discussed the relationships among the local seismicity, the Mw 7.5 earthquake, hidden faults, and the upward migrating fluid. Investigations into this devastating Mw 7.5 earthquake are crucial for understanding the influence of the crustal fluids on fault behavior.

For the Noto peninsula earthquake, most source inversion studies (Fujii and Satake, 2024; Okuwaki et al., 2024; Ma et al., 2024; Xu et al., 2024; Yamada et al., 2025) have assumed two-segment rupture models involving both southeast- and northwest-dipping faults, reflecting the complex fault system in the source region inferred from the comprehensive seismic and geological surveys (MEXT, 2021). The aftershock distribution determined by the JMA automatic catalog (JMA, 2024a) aligns with the JSPJ fault model (Figure 1), supporting the hypothesis of multiple fault planes of earlier studies (Okuwaki et al., 2024; Ma et al., 2024; Xu et al., 2024). In contrast, Liu et al. (2024) modeled the kinematic rupture process using a single fault plane, based on near-field strong motion records, teleseismic body-waves, and GNSS data, raising a critical question regarding the reliability of fault geometry constraints derived from seismic and geodetic observations. Thus, the degree of complexity in the source fault system remains a subject of ongoing debate.

The frequency dependence of seismic radiation has been widely discussed in source process studies (Koper et al., 2011; Yagi et al., 2012). Low-frequency signals are particularly useful for imaging the macroscopic rupture process, as they are sensitive to regions of large slip. In contrast, high-frequency seismic energy radiation is essential for understanding the complexities of the seismic source process and fault geometry. Previous studies including theoretical analysis, laboratory experiment, and seismic waveform analysis have shown that high-frequency P-waves can be radiated from abrupt changes in slip and/or rupture velocity along the fault plane (e.g., Bernard and Madariaga, 1984; Beresnev, 2017), as well as from the structural heterogeneities such as the fault barriers and branching (e.g., Adda-Bedia and Madariaga, 2008; Bruhat et al., 2016). Furthermore, classical studies have suggested that high-frequency radiation is often associated with rupture termination, known as the stopping phase (e.g., Savage, 1965; Bernard and Madariaga, 1984). Therefore, high-frequency seismic waves are essential for understanding the complexity of rupture processes and the geometry of fault systems.

For the Noto peninsula earthquake, Honda et al. (2024) applied an array-based back-projection method to S-wave records obtained from a local seismic array in Nagano Prefecture (SK-net) combined with K-NET/KiK-net data operated by the National Research Institute for Earth Science and Disaster Resilience (NIED) (Aoi et al., 2020). They analyzed two frequency bands (0.05–2.0 Hz and 0.5–5.0 Hz) and found frequency-dependent seismic radiation from a three-segment fault system, suggesting that variations in fault dip direction may correspond to the observed high-frequency radiation.

In this study, we investigate the frequency-dependent seismic-wave radiation processes using the back-projection (BP) of teleseismic P-waves across multiple frequency ranges. By analyzing the temporal evolution of BP images for different frequency ranges, we explore the relationship between high-frequency seismic wave radiation and the large-scale rupture process inferred from lower-frequency P-wave radiation. Simultaneous observation of both high- and low-frequency teleseismic P-waves enables a more comprehensive understanding of rupture process across wide frequency ranges. Moreover, the frequency-dependent seismic radiation images provide important constraints on the geometry of the complex source fault system.

2. Data and Method

The JMA catalog lists this earthquake as two distinct events: M_{jma} 5.9 at 7:10:9.54 UTC and M_{jma} 7.6 at 7:10:22.57 UTC (JMA, 2024a,b). Here, M_{jma} denotes the JMA magnitude scale based on observed amplitudes of displacement and/or velocity waveforms (JMA, 2024b). These were also observed in near-field strong-motion records (Liu et al., 2024). For simplicity, we treat them as the Mw 7.5 earthquake sequence at 7:10:10 (UTC) (JMA, 2024a) in our BP analysis with teleseismic records. In the Discussion, we revisit the possible two-event nature of this sequence based on our BP results.

2.1. Multi-frequency Teleseismic P-wave

We used three-component seismograms at global seismic stations downloaded from the IRIS Data Management Center. Prior to waveform processing, we removed the instrument response from the raw data, converted them to displacement waveforms, and resampled them at 0.1 s intervals.

Our data selection method generally follows Tarumi and Yoshizawa (2023), originally developed for identifying coherent receiver functions (Tkalčić et al., 2011). First, we selected seismic stations located between 30° and 95° from the epicenter, targeting teleseismic P-waves. Next, we calculated cross-correlation coefficients (CC) and lag-times within a 30 s window centered on the theoretical P-wave arrival time (± 15 s), based on the AK135 model. For each observed waveform, displacement records with CC > 0.7 were grouped, and the group with the largest number of waveforms was used for the back-projection analysis. The estimated lag-times via the cross-correlation analysis were also used for travel-time corrections to account for 3-D structural effects, following (Tarumi and Yoshizawa, 2023).

To estimate the frequency-dependent seismic radiation, we applied band-pass filters to three-component seismograms with multiple frequency ranges: 0.03-0.3 Hz, 0.05-0.5 Hz, 0.1-1.0 Hz, and 0.3-2.0 Hz. The waveform-selection process described above was conducted independently for each frequency range. Figure 2 shows an example of our teleseismic dataset for the lowest-frequency range (0.03-0.3 Hz), while datasets for the other frequency bands are provided in Figures S1-S3 in Supplementary Material. For all frequency bands, our teleseismic datasets exhibit good azimuthal coverage (e.g., Figure 2). A theoretical study by Fukahata et al. (2014) demonstrated that the BP can be performed effectively when the stacked Green's function approximates a delta function, a condition enabled by good azimuthal coverage. Our dataset (Figures 2, S1–S3) satisfies this condition reasonably well, providing stable BP images (e.g., Okuwaki et al., 2014; Kiser and Ishii, 2016; Okuwaki et al., 2018).

2.2. Back Projection with LQT coordinate system

Seismic back-projection (BP) analysis time-reverses observed seismograms to the source time and locations from which the target seismic phase is radiated. The BP analysis has the advantage of capturing the high-frequency radiators (e.g., Kiser and Ishii, 2013; Okuwaki et al., 2018; Mai et al., 2023), which is essential for understanding complex rupture processes. Although seismic waveform inversion is a powerful method for estimating the spatiotemporal distribution of moment release, it is hard to incorporate high-frequency waves due to the high computational cost of computing Green's functions and uncertainties in the fine-scale 3-D structures. Moreover, the inversion requires a priori assumptions, such as the predefined fault geometry, making it challenging to assess the influence of complex fault networks

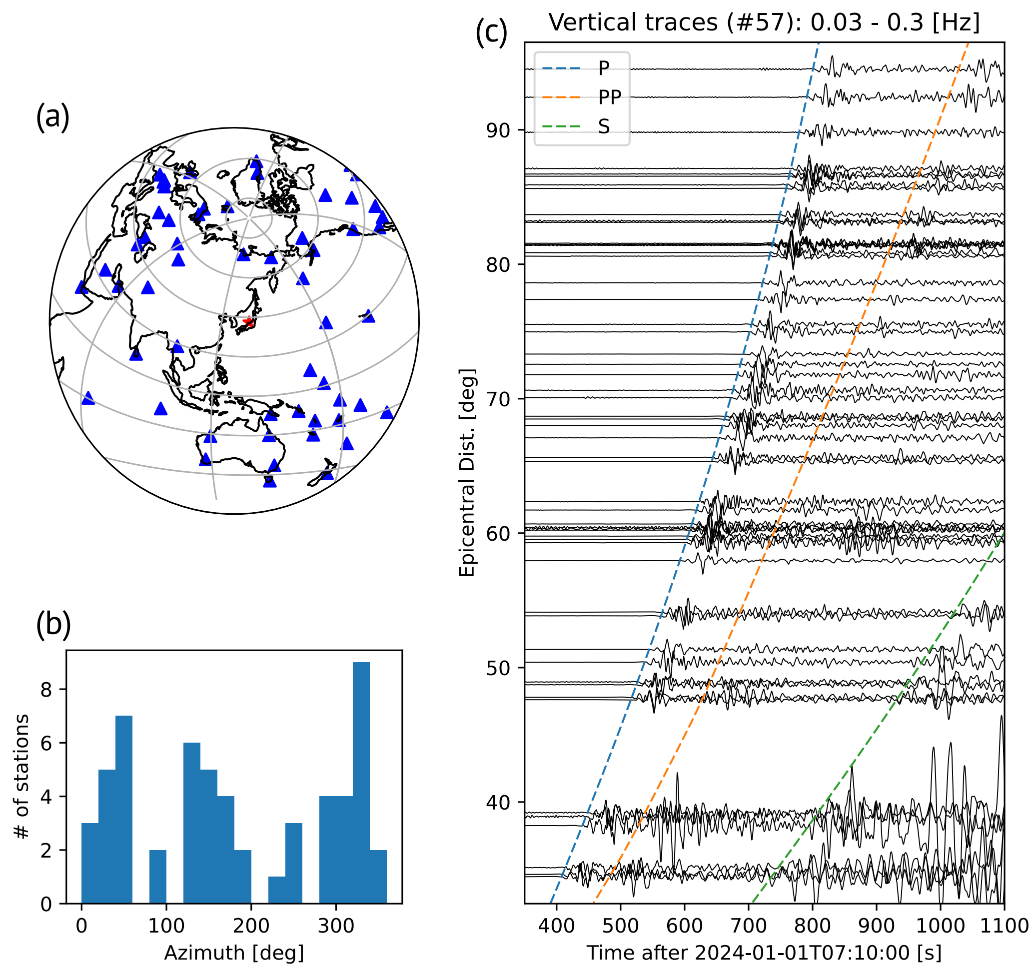

Figure 2: Teleseismic waveform dataset used for the BP analysis with a frequency range of 0.03-0.3 Hz. (a) Map of the stations used. The red and blue triangles indicate the hypocenter and seismic stations, respectively. (b) Histogram of the azimuths from the source to the stations. (c) Vertical-component seismograms, scaled by the maximum amplitude of direct P phase. The blue, orange, and green lines represent the travel-time curves for P, PP, and S waves, respectively.

on the source process. The teleseismic P-wave BP analysis thus provides an effective alternative approach for imaging frequency-dependent radiation and constraining high-frequency emissions.

BP analysis has generally been performed using the vertical-component seismograms (e.g., Ishii et al., 2007; Kiser and Ishii, 2013; Xu et al., 2009; Okuwaki et al., 2014; Tarumi and Yoshizawa, 2023), as teleseismic P-waves are primarily recorded in the vertical component. However, the particle motion of teleseismic P-waves is inclined, involving some amount of signals in the horizontal (radial) component, even at epicentral distances of around 90°. This inclination increases at stations closer to the source. Thus, to consider the total amplitude of P-waves, it is preferable to incorporate the two horizontal components in addition to the vertical component. In this study, we employ the LQT coordinate system (also known as the ray-coordinate system) (Vinnik, 1977) to implement the BP analysis (hereafter referred to as the LQT-BP method). Figure S4 illustrates the ray-coordinate system. This new coordinate system, commonly used in receiver function studies (e.g., Kind and Yuan, 2011), is derived by rotating the three-component seismograms into the direction of the P-wave incidence (L), the perpendicular direction to the L-component (Q), and the transverse direction (T) (Vinnik, 1977) (Figure S4). The use of the LQT system enhances the direct P-wave signal, potentially leading to more refined BP images.

In our BP analyses, we utilized the N-th root stacking method (Rost and Thomas, 2002), which effectively enhances coherent signals. This robust stacking approach has been applied in many previous BP studies (Xu et al., 2009; Honda et al., 2011; Tarumi and Yoshizawa, 2023), enabling us to suppress noises and to enhance the BP images for target signals, such as P-waves.

Our LQT-BP analysis can be formulated as follows,

$$L'_j(t, \mathbf{x}_j) = \frac{1}{M} \sum_{i=1}^{M} \mid l_i(t + \tau_{ij}) \mid^{\frac{1}{N}} \cdot \mathrm{sgn}(l_i(t + \tau_{ij})) \tag{1}$$

$$L_j(t, \mathbf{x}_j) = \mid l_j(t) \mid^{N} \cdot \mathrm{sgn}(L'_j(t, \mathbf{x}_j)) \tag{2}$$

where M is the number of stations, τ_{ij} the predicted arrival time between the i-th station and the j-th source grid, l_i an L-component seismogram at the i-th station, $\mathbf{x}_j$ the coordinate point of j-th source grid, and $L_j(t)$ the stack of L-component waveforms at the j-th source grid associated with the total radiation power of seismic waves. In this study, we adopted $N = 4$ for all frequency ranges. Finally, to extract the spatiotemporal radiation intensity $BP(t, \mathbf{x}_j)$, we integrate $L_j(t, \mathbf{x}_j)$ as follows,

$$BP(t, \mathbf{x}_j) = \frac{1}{\delta t} \int_{t-\delta t}^{t+\delta t} L_j(t', \mathbf{x}_j) dt', \tag{3}$$

where δt represents an integration interval. In this study, the interval is adaptively defined as half of the averaged period T' for each frequency range, with a minimum δt of 1 second.

The LQT-BP method requires both the travel time and the incident angle of the P-wave before stacking (eqs. (1) and (2)). To calculate the theoretical arrival times and incident angles of P-waves, we used a 1-D spherical structure model AK135 (Kennett et al., 1995). Potential source grids are distributed between $-1.5°$ and $+1.5°$ around the epicenter (E137.2, N37.5) at a depth of 10 km, sufficiently covering the potential source region (Figure 1). The source grid interval is set to 0.05°, except for the highest frequency range (0.3–2.0 Hz), where it is reduced to 0.015° to take account of the shorter wavelength.

3. Results

Our BP analysis successfully estimated the frequency-dependent P-wave radiation process. The results are displayed in Figures 3 and 4, as well as in Supplementary Movie S1. Figure 3 presents the multi-frequency BP snapshots at 5-second intervals, with the fault models from the Japan Sea Earthquake and Tsunami Project (JSPJ; MEXT (2021)) superimposed. Figure 4 shows the temporal evolution of P-waves radiation power for each frequency band, normalized by the maximum amplitude of the lowest-frequency signal (the blue line in Figure 4). Figure 5 shows the time evolution of P-wave radiation, projected along the N60°E line, with the projected points indicated in Figure S5.

Across all frequency ranges, the radiation areas cover the JSPJ fault model (black dotted squares in Figures 3). The P-wave radiation extended from the epicenter toward the western inland and eastern offshore regions

(Figure 3) and persisted for approximately 44 s, with peak radiations occurring 30-40 s after the origin time (07:10:10 UTC, (JMA, 2024a)) (Figure 4). The radiation sequence can be divided into four main episodes (Figures 5): [E1] initial radiation near the hypocenter (0–18 s), [E2] intense high-frequency radiation between the initial stage and the subsequent main radiation phases (18–28 s), [E3] strong radiation in the inland region of the Noto Peninsula (25-44 s), and [E4] significant radiation in the eastern offshore region (25-44s). Hereafter, in each episode, relatively higher-frequency P-wave radiations are denoted with a superscript prime (e.g., $E1'$ for higher frequency signals corresponding to the first episode, E1).

The rupture episodes characterized by low-frequency radiation are consistent with previous studies using teleseismic P-waves (Okuwaki et al., 2024; Kutschera et al., 2024; Ma et al., 2024; Xu et al., 2024; Liu et al., 2024), which identified bilateral rupture propagation from the hypocenter toward the southwest inland and eastern offshore regions over approximately 40 s. The time series of low-frequency BP amplitude shown in Figure 4 is comparable to the temporal moment-release derived from these inversion studies, although they do not necessarily correspond directly. Figure S6 shows the cumulative radiation integrated over 44 s from the origin time (2024-01-01T7:10.10 UTC) of each frequency band. Except for the highest frequency range, 60 % of the cumulative radiation power overlaps the aftershock distribution (Figure S6 (e)), clearly illustrating the bilateral migration of source radiation.

However, prior to the main bilateral migration, during [E2], high-frequency P-waves (0.1–1.0 Hz and 0.3–2.0 Hz, E2$'$) were radiated intensely from the hypocentral area between 18–25 s, despite the absence of low-frequency energy (Figures 3, 4, and 5), a distinct feature of this Mw 7.5 earthquake. Other teleseismic BP results based on array analyses using high-frequency P-waves (Ma et al., 2024; Xu et al., 2024) are generally consistent with our images in the higher-frequency bands (0.1–1.0 Hz; 0.3–2.0 Hz). In particular, the northeastern high-frequency radiators identified in this study are also seen in the results using arrays in North America and Australia (Xu et al., 2024; Ma et al., 2024), but not in those using the array in Europe (Xu et al., 2024). While such consistencies exist, the differences between our and other teleseismic BP results may arise from variations in station-source geometry.

Figure S7 displays the BP results derived from conventional BP imaging using only the vertical component of P-waves. The LQT-BP results (Figures 3 and 4) resemble those from the traditional BP (Figure S7), but the LQT-BP method slightly enhances the P-wave sources, suggesting that the ray-coordinate system (Figure S4) allows us to extract P-wave amplitudes effectively. Still, for the discussion of the source rupture process, the choice of a coordinate system for stacking seismograms seems not to be critical.

Figures S8–S10 show the dependence of BP images on the N parameter in eqs. (1) and (2). At lower N ($N = 1, 2$; Figures S8 and S9), prominent sidelobes appear around the main lobes, though the main features remain robust regardless of N. In contrast, higher N (Figures S8 (c) and 3) effectively suppresses side-lobes and enhances the main BP signals.

3.1. E1: Initial radiation around the hypocenter (0–18 s)

This episode corresponds to the initial rupture stage of the Mw 7.5 earthquake in the hypocentral area. At this initial stage, relatively high-frequency P-wave radiation (0.3–2.0 Hz, E1$'$) is observed preceding the low-frequency component near the hypocenter during the first 0–10 s (Figures 3 (d), 5 (d)). Between 10 and 15 s, the main seismic radiation shifts to the lower-frequency range (0.05-0.5 Hz), which becomes the dominant seismic energy source at this stage. Although minor southwestward radiation is seen in the lowest-frequency band (0.03–0.3 Hz; Figures 3 (a) and 5 (a)), this feature was not observed in the near-field S-wave BP results (Honda et al., 2024), and is likely a ghost artifact of BP. The seismic radiation then fades (Figures 3 (b) and 5 (b)). Overall, during this stage (up to 18 s), the migration speed of the radiation is very low, estimated to be less than 2 km/s. The early stage of this episode (0–10 s) may correspond to the initial quiet slip and slow rupture process identified in previous waveform inversion studies (Okuwaki et al., 2024; Ma et al., 2024; Xu et al., 2024; Liu et al., 2024).

3.2. E2: High-frequency radiation lacking low-frequency (18–28 s)

Between 18 and 28 s, intense high-frequency P-waves radiation (0.1–2.0 Hz, E2$'$) emerges from the hypocentral region, while low-frequency P-waves (0.03–0.5 Hz) are notably absent. This frequency-dependent behavior is

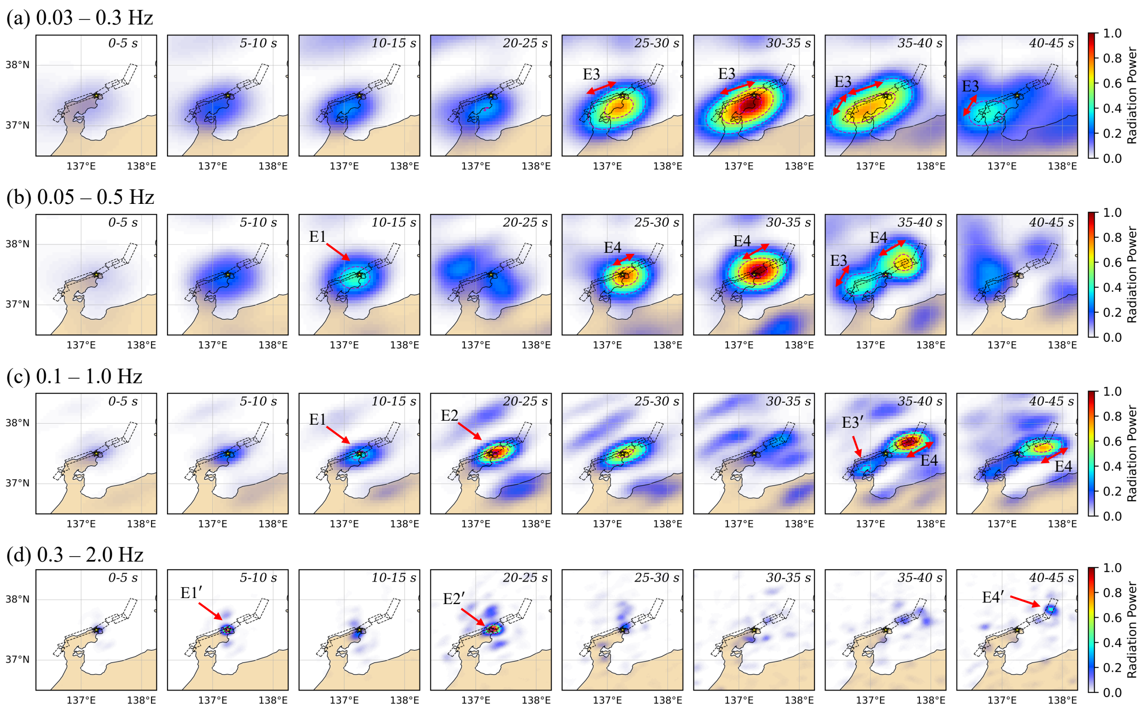

Figure 3: BP snapshots with 5-second intervals for multiple frequency bands: (a) 0.03–0.3 Hz, (b) 0.05–0.5 Hz, (c) 0.1–1.0 Hz, and (d) 0.3–2.0 Hz. Rectangles with black dotted lines represent the fault models from the JSPJ (MEXT, 2021), NT2, NT3, NT4, NT5, NT6, NT8, and NT9, marked in Figure 1. Note that NT2 and NT3 dip northwestward, while the others dip in the opposite direction (see Figure 1). Yellow stars indicate the epicenter of the Mw 7.5 event (USGS, 2024), which occurred at 07:10:10 (UTC). Magenta thin contour lines show radiation intensities at 30 %, 60 %, and 90 %. Radiation power is normalized to the maximum value for each frequency band. The red arrows highlight the locations of notable higher-frequency (HF) radiation (E1′, E2′, E3′, and E4′) and the corresponding lower-frequency radiation (E1, E2, E3, and E4).

reflected in the time-dependent radiation power (Figure 4). The highest-frequency P-wave radiation is concentrated around the hypocenter between 18 and 25 s (E2$'$), during which low-frequency radiation temporarily ceases (Figures 3, 4, and 5), creating a hole in the low-frequency radiation. During this gap, the high-frequency component (0.1–2.0 Hz) dominates the total radiation power (Figure 4). This distinct high-frequency radiation may be essential to understanding the rupture process of this Mw 7.5 earthquake, possibly serving as a bridge between the initial stage (E1) and the main rupture stages (E3 and E4).

3.3. E3: Intense radiation in the inland of the Noto Peninsula (25–44 s)

This episode represents one of the most significant stages of seismic radiation, extending across the entire peninsula (Figure 3 (a)). The dominant frequency content of this episode is in the lowest frequency range (0.03-0.3 Hz) of our analysis. The substantial low-frequency radiation propagates toward the southwestern inland areas of the Noto Peninsula from 25 to 44 s (Figure 3 (a)). From 28 s to 40 s, the low-frequency P-wave radiation reaches its peak intensity, representing the most powerful phase of this Mw 7.5 earthquake (Figures 3 and 5). This intense low-frequency radiation may have contributed to the destructive damage in the inland areas of the peninsula. The migration speed of the fault rupture area between 28 and 35 s is estimated to be approximately 3.0 km/s (Figure 5). This stage notably lacks high-frequency signals, but after 40 s, the low-frequency radiation gradu-

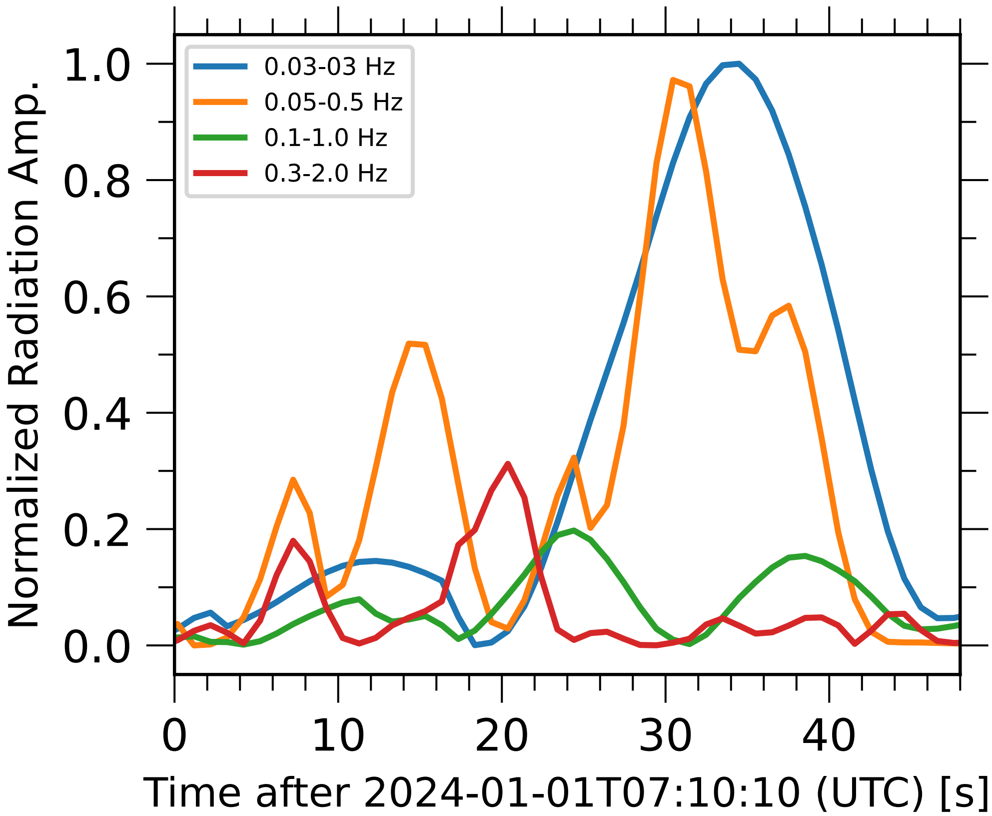

Figure 4: P-wave radiation power as a function of time for multiple frequency bands, normalized to the maximum amplitude in the 0.03-0.3 Hz band. Colored lines represent different frequency ranges: blue (0.03–0.3 Hz), orange (0.05–0.5 Hz), green (0.1–1.0 Hz), and red (0.3–2.0 Hz).

ally diminishes, accompanied by a weak emission of higher-frequency signals (0.1–1.0 Hz, E3$'$) near the southwestern tip of the peninsula (Figures 3 and 5).

3.4. E4: Intense radiation in the eastern offshore region (25–44 s)

E4 corresponds to intense radiation in the eastern offshore region, primarily in the frequency ranges of 0.05-0.5 Hz and 0.1–1.0 Hz (Figures 3 and 5). During this stage, the P-wave radiation source propagates from the hypocentral area toward the eastern offshore region (from 20 to 25 s), peaking at 30–35 s in the offshore regions, similar to the inland radiation in E3 (Figures 3, 4, and 5). This stage likely involves shallow fault rupture, as suggested by previous inversion studies (Okuwaki et al., 2024; Xu et al., 2024; Ma et al., 2024; Liu et al., 2024), which may have reached the surface (Gabuchian et al., 2017), potentially contributing to tsunami generation. The estimated rupture speed during this stage is slower than that in E3, at less than 3.0 km/s (Figure 5). Around 38 s, seismic radiation abruptly ceases, followed by a notable increase in higher-frequency P-wave emissions (E4$'$ in Figures 3, 4, and 5). This frequency transition occurs near the eastern offshore fault segment (N2) (Figure 3 (c,d)).

4. Discussion

The resultant BP images reveal a notable frequency dependence, indicating significant complexity in the seismic radiation processes of this Mw 7.5

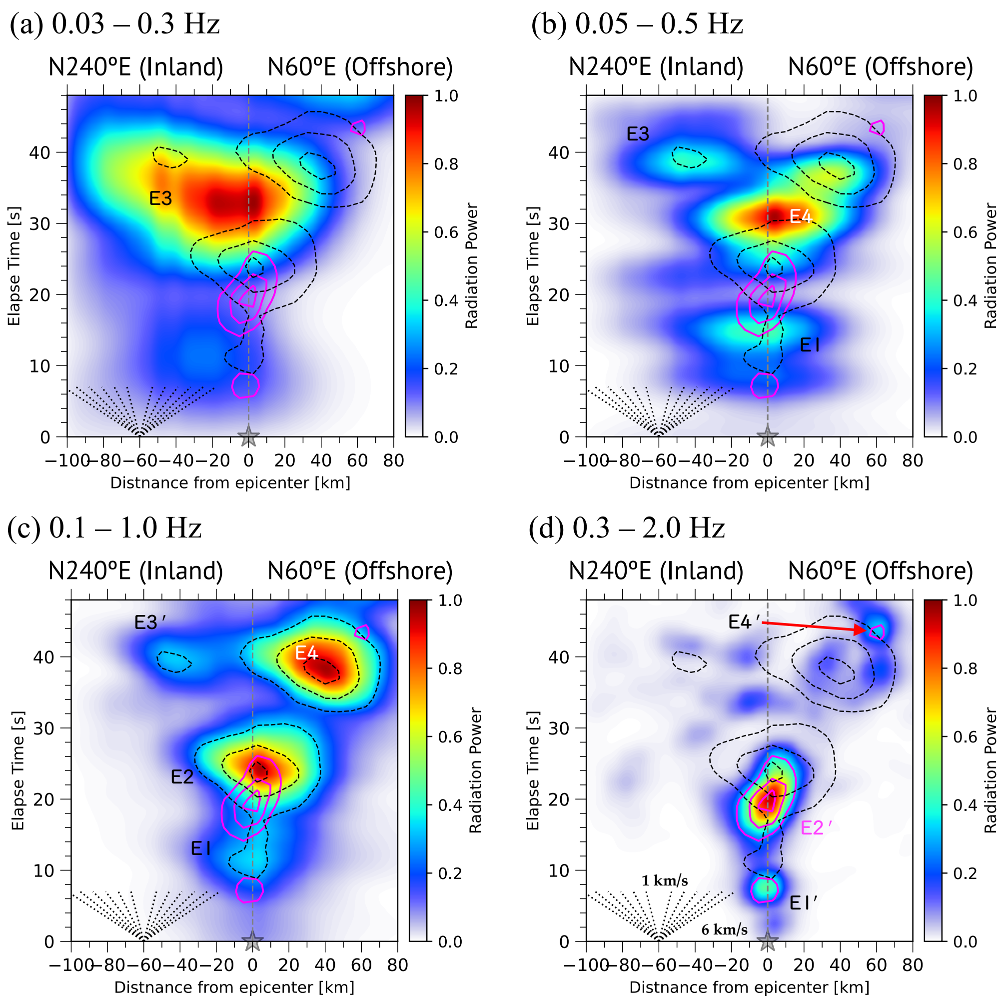

Figure 5: Time evolution of P-wave radiation projected along the N60°E line for multiple frequency bands: (a) 0.03–0.3 Hz, (b) 0.05–0.5 Hz, (c) 0.1–1.0 Hz, (d) 0.3–2.0 Hz. Gray stars represent the epicenter. Vertical dashed lines divide the positive and negative sides in the horizontal axis, corresponding to the northeast offshore and southwest inland parts of the Noto Peninsula, respectively. Dashed lines in the lower left indicate rupture velocities, ranging from 1.0 to 6.0 km/s. E1, E2, E3, and E4 represent the radiation episodes identified in this study. In all panels, black and magenta contour lines indicate 30 %, 60 %, and 90 % of the highest-frequency radiation (black dashed: 0.1–1.0 Hz, magenta solid: 0.3–2.0 Hz).

earthquake. These complex source processes may be attributed to crustal fluids that have driven long-term seismic swarms in this region since November 2020 (Amezawa et al., 2023). Nishimura et al. (2023) proposed that the upward migration of fluids weakened fault strength, generating the preceding seismic swarms in the Noto peninsula. Yoshida et al. (2024) suggested that the crustal fluid may have triggered the main rupture process associated with E3 and E4 in this study. Additionally, Nakajima (2022) reported a high Vp/Vs ratio in the lower crust beneath the hypocentral area, indicating fluid-rich material.

The source region of this destructive event comprises a complex fault system, as inferred from detailed investigations including comprehensive field surveys (MEXT, 2021) (Figure 1). While the southwestern faults dip to the southeast, those in the northeastern offshore region dip in the opposite direction to the northwest (Figures 1 and MEXT (2021)), as supported by the aftershock distribution (Figures 1 and JMA (2024a)). Relocated seismicity further revealed a fault system with multiple hidden faults (Yoshida et al., 2024), suggesting that the hypocentral area likely involves at least three intersecting fault segments.

In this section, we first compare our frequency-dependent seismic radiation process with near-field BP (Honda et al., 2024) and observations. We then examine the origin of prominent high-frequency emissions associated with small-scale source complexities, followed by discussion of the broader frequency-dependent characteristics revealed by our BP analysis.

4.1. Comparison with the near-field BP results and observations

Unlike previous studies using teleseismic data (e.g., Okuwaki et al., 2024; Kutschera et al., 2024; Ma et al., 2024; Xu et al., 2024; Liu et al., 2024), this study reveals frequency-dependent characteristics in P-wave radiation from the complicated rupture process. Similar features are observed in S-wave radiation inferred from the near-field strong motion data by Honda et al. (2024), who applied array-based BP analysis to S-wave records in two frequency bands (0.05–2.0 Hz; 0.5–5.0 Hz), using travel-time calculations based on a 3-D velocity model (Matsubara et al., 2022). The teleseismic and near-field BP results are generally consistent, although discrepancies may arise due to differences in the target phases (P vs. S), propagation-path effects (e.g., scattering, attenuation), and a priori assumptions.

Our results in Figures 3 and 5 suggest that the low-frequency radiation dominates along southeast-dipping faults (NT9, NT8, NT6, NT5, and NT4 in Figure 1), consistent with the near-field BP modeling (Honda et al., 2024). In contrast, the northwest-dipping faults (NT3 and NT2 in Figure 1) generate higher-frequency signals (0.1–1.0 Hz) during 36–42 s after rupture initiation, though with much weaker amplitude than lower-frequency (Figure 4). While the causes of this frequency variation is discussed later, the high-frequency radiation from the northwest-dipping faults is approximately one-eighth the peak power of the low-frequency radiation from southeast-dipping faults (0.03–0.3 Hz; Figure 4), in line with the one-tenth estimated by Honda et al. (2024) using different frequency ranges. These findings suggest that lower-frequency radiation is mainly associated with faults having consistent dip direction and is less efficiently generated across transitions between oppositely dipping faults.

Figure S11 displays selected near-field velocity waveforms derived from high-pass-filtered (0.03 Hz) accelerograms at ISK001 and ISKH02 (borehole records), and ISK015, aligned along the inland rupture propagation path (Figure S11 (a)). Arrows in Figure S11 (b–c) mark the timing of fault rupture beneath each station, as inferred from our BP results. Episode E1, near the epicenter, is consistent with the near-field records at ISK001 (Figure S11 (b, c)). After E2, a long-period velocity pulse appears at ISK001 (Figure S11 (b)), and clear E3 phases are seen at ISKH02 and ISK015 (Figure S11 (c, d)). The frequency variation seen in these near-field records reflects our BP results; for example, high-frequency components are concentrated between the end of E1 and the onset of E3 at ISKH02 (Figure S11 (c)).

4.2. Sources of higher-frequency P-waves

In this section, we examine the sources of the prominent high-frequency P-waves (0.3–2.0 Hz), E1$'$, E2$'$, and E4$'$. Such high-frequency radiation generally reflects complex, smaller-scale fault processes rather than the macroscopic rupture propagation.

High-frequency seismic signals are typically generated by rapid changes in rupture and/or slip velocity, complex fault branching, and interactions with fault barriers and asperities (e.g., Savage, 1965; Madariaga, 1977; Bernard and Madariaga, 1984; Madariaga, 2003; Adda-Bedia and Madariaga, 2008; Beresnev, 2017; Marty et al., 2019), all of which are essential for understanding the complexity of this earthquake. As noted in Section 2, the JMA earthquake catalog (JMA, 2024a) registers two distinct events: M_{jma} 5.9 (07:10:09.54 UTC) and M_{jma} 7.6 (07:10:22.57 UTC). While we treated them as a single Mw 7.5 event for data processing in the BP analysis (based on GCMT catalog), in this section we extend the discussion to consider both events (M_{jma} 5.9 and M_{jma} 7.6), hereafter referred to as the Mw 7.5 earthquake sequence.

4.2.1. E1′: Starting phase of this Earthquake

The first instance of high-frequency radiation, $E1'$ (Figure 5), likely represents the initiation of the fault rupture process or the starting phase (Madariaga, 1977). At rupture onset, substantial energy is required to rapidly accelerate slip, which generates strong high-frequency radiation (Madariaga, 1983). $E1'$ precedes the lower-frequency radiation (0.05–1.0 Hz) concentrated near the hypocentral region (Figure 5), suggesting that it may have facilitated the subsequent rupture process in E1 corresponding to the initial stage of this Mw 7.5 earthquake sequence. Meanwhile, as noted earlier, the JMA catalog lists a smaller foreshock (M_{jma} 5.9) at 07:10:09.54 UTC (JMA, 2024a), which may have triggered $E1'$ and its subsequent rupture growth, although this potential relationship cannot be fully resolved by our teleseismic BP analysis.

Following this initiation phase, the region radiating P-waves during E1 does not expand significantly (Figure 3), with an estimated propagation speed of about 1 km/s (Figure 5), which is consistent with the slow-rupture episode reported in previous studies (e.g., Okuwaki et al., 2024; Ma et al., 2024; Liu et al., 2024). The presence of crustal fluid near the hypocenter (Nakajima, 2022) may inhibit rupture acceleration. These observations support the hypothesis of fluid-induced slow rupture initiation, as predicted by numerical and theoretical studies (e.g., Rice, 1992; Marguin and Simpson, 2023), and are consistent with the high-frequency radiation during this phase (Ma et al., 2024).

4.2.2. E2′: Triggering the low-frequency radiation of E2, E3 and E4

The second episode of high-frequency seismic emission (E2′ in Figure 5 (d)) likely reflects a secondary initiation within the Mw 7.5 earthquake sequence. The larger event occurred about 10–15 s after the smaller M_{jma} 5.9 foreshock (JMA, 2024a). Near-field strong motion records also suggest a 15–20 s delay after the excitation of the M_{jma} 5.9 event (e.g., Liu et al., 2024). The timing of E2′ inferred in this study roughly coincides with the origin time of the M_{jma} 7.6 mainshock. E2 is also observed in the high-frequency BP results using near-field S-wave data (Honda et al., 2024), although its timing does not perfectly match our teleseismic results. Yoshida et al. (2024) relocated the two distinct but spatially close events, suggesting that both the M_{jma} 5.9 foreshock and the M_{jma} 7.6 mainshock occurred on the same fault plane. Thus, although the teleseismic records may be affected by uncertainties, $E2'$ in our BP results likely corresponds to the onset of the bilateral rupture stage within the Mw 7.5 earthquake sequence.

Crustal fluids, identified by an anomalously high Vp/Vs ratio near the E2 region (Figure 3 (c, d)) (Nakajima, 2022), likely influenced the source characteristics of E2. Yoshida et al. (2024) suggested that the foreshock triggered the mainshock through the upward fluid migration, while Ma et al. (2024) suggested that this earthquake sequence began with a slow rupture in a fluid-rich zone, followed by a faster rupture in a drier region. This sequence may be reflected in our BP images: E1 corresponds to the initial slow rupture, transitioning into the faster bilateral rupture propagation of E3 and E4 toward the west and east, respectively (Figures 3 and 5). The higher-frequency event E2 appears to mark this transition (Figures 3, 4, and 5), acting as a bridge across the abrupt change in rupture speed. While such a transition can occur without elevated pore pressure (e.g., Bruhat et al., 2016), the presence of fluids may facilitate more efficient rupture acceleration (Pampillón et al., 2023). Thus, the higher-frequency radiation observed in E2 may result from a combination of abrupt rupture speed changes induced by fluid migration and the onset of the major rupture expansion in this earthquake sequence.

Although the complexity of fault geometry may also play a role (MEXT, 2021; Yoshida et al., 2024; Okuwaki et al., 2024), the lack of high-frequency P-wave radiation during E3 and E4 (except for a minor emission at the end of E4) may indicate limited influence from the complex fault network or heterogeneities such as fault barriers.

4.2.3. E4′: Stopping phase of E4

The fourth high-frequency emission event (E4′ in Figures 3 (d) and 5 (d)) likely represents the stopping phase of fault rupture in the northeastern offshore area of the Noto Peninsula, coinciding with the location of the offshore fault N2 (MEXT, 2021) shown in Figure 1. Classical studies have shown that abrupt rupture termination can effectively generate high-frequency seismic energy (Savage, 1965; Madariaga, 1977). Fault slip models by Fujii and Satake (2024) and Mizutani et al. (2024), based on geodetic and tsunami waveform data, suggested that the northeastern offshore fault N2 did not slip. Besides, seismic waveform inversions including the near-field data (Ma et al., 2024; Xu et al., 2024; Liu et al., 2024) found minimal slip on the northeastern offshore fault patch. These observations agree well with our results, which indicate a stopping phase at the northeastern end of the source region near the N2 fault.

4.3. Frequency-dependent P-wave radiation and complex fault rupture process

The most prominent P-wave radiation observed in this study occurs in the lowest-frequency range (0.03–0.3 Hz) in the inland regions of this peninsula (E3), while another notable low- to intermediate-frequency (0.05–0.5 Hz) radiation mainly originates from the northeastern offshore region (E4) (Figure 3 (a, b)). Note that intense high-frequency components (0.1–2.0 Hz) precede these dominant lower-frequency radiations. In this subsection, we discuss the relationship between these lower- and higher-frequency radiation processes in more detail, considering the multi-segmented fault connections identified by the field surveys, including submarine reflectivity explorations (MEXT, 2021) .

A distinct transition in the frequency content of radiated P-waves from high (0.1–2.0 Hz) to low (0.03–0.5 Hz) frequencies after 18 seconds is clearly shown in Figures 3 and 5. E3 appears to be triggered by the high-frequency emission event E2 and transitions smoothly into an intense low-frequency emission (0.03–0.3 Hz) (Figures 3 and 5). Notably, after this frequency shift, E3 exhibits little higher-frequency radiation and gradually fades after 40 s (Figures 3 and 5) . This behavior is likely associated with large near-surface slip, as inferred from the previous waveform inversion studies (Okuwaki et al., 2024; Ma et al., 2024; Xu et al., 2024; Liu et al., 2024). Shallow fault slips are often characterized by longer rise times, as observed in other inland earthquakes (e.g., Ji et al., 2015; Hao et al., 2017). Although the exact depth of the P-wave source remains undetermined due to the limited vertical resolution of BP analysis, the lower-frequency P-wave radiation in the southwestern inland region persists longer than in other areas (Figure 3 and 5). Consequently, the lack of high-frequency radiation in E3 may result from lower slip rates at shallow depths, potentially further suppressed by crustal fluids. In addition, the very shallow thrust fault may have interacted with the ocean bottom, contributing to enhance low-frequency seismic emission (e.g., Gabuchian et al., 2017).

At the end of E3, relatively higher-frequency energy (0.05–0.5 Hz and 0.1–1.0 Hz) are emitted from the southwestern tip of the peninsula (E3$'$ in Figures 3 and 5), which can be interpreted as the stopping phase of E3. However, this termination does not involve the highest-frequency P-wave, which instead appears in E4. In the recent tomographic model (Nakajima, 2022), an anomalously high Vp/Vs ratio was observed in the southwestern area of the Noto Peninsula. A plausible explanation for this stopping phase without higher-frequency emission could be the fluid-rich conditions in this region (Noda and Lapusta, 2013; Madden et al., 2022).

Meanwhile, from E2 to E4, the frequency components of radiated P-waves evolve continuously. E4 can also be triggered by E2, after which the frequency range of emitted P-waves gradually shifts to lower frequencies (0.05–0.5 Hz) (Figures 3 and 5), possibly reflecting the evolution process of fault rupture propagation. After around 36 s, an opposite transition occurs, with the main frequency range smoothly shifting from low to high frequencies (Figures 3 and 5).

A plausible cause of the frequency transition observed toward the end of E4 is the complex fault geometry. The JSPJ model (MEXT, 2021) and aftershock distribution (Figure 1 and JMA (2024a)) suggest a multi-segmented fault system in the source region. Seismic inversion studies that treated fault geometry as unknown parameters (Okuwaki et al., 2024; Kutschera et al., 2024) indicate differences in strike between the southwestern inland

and northeastern offshore faults. Other seismic inversion studies incorporating tsunami and geodetic data also adopted multi-segmented fault models (Fujii and Satake, 2024; Mizutani et al., 2024; Xu et al., 2024; Yamada et al., 2025; Mizutani et al., 2024). A comparison of the two frequency bands (0.05–0.5 Hz and 0.1–1.0 Hz) in Figure 3 (b, c) indicates that, between 35-45 s, lower-frequency radiation (0.05-0.5 Hz) originates near NT4, while higher-frequency radiation (0.1-1.0 Hz) arises near NT3, despite the limited resolution of teleseismic P-wave data. Similar high-frequency radiators have been identified in BP studies using teleseismic P-waves (Xu et al., 2024; Ma et al., 2024) and near-field S-waves (Honda et al., 2024), near the NT3 and NT4 faults. These two faults have opposite dipping directions (Figure 1 and MEXT (2021)), and our frequency-dependent BP results indicate that the P-wave radiators coincides with the fault branching point in the JSPJ model (MEXT, 2021). This frequency transition at the end of E4 likely reflects rupture propagation across a complex, multi-segmented fault system.

In contrast, Liu et al. (2024) showed that a single planar fault-slip model could explain multiple geophysical datasets. Their study highlights an intrinsic limitation: geophysical observations alone (including seismic and geodetic data) may not adequately constrain fault geometry. Nevertheless, for the Mw 7.5 Noto Peninsula earthquake sequence, a multi-segmented fault model appears more plausible, supported by the JSPJ surveys (MEXT, 2021), the dense aftershock distribution (JMA, 2024a) (Figure 1), and the frequency transitions observed in our BP results, which were obtained without any a priori assumptions on fault geometry. However, uncertainty in fault geometry and its implications for source inversion remains a major challenge and warrants further investigation.

Thus, the observed frequency-dependent P-wave radiation sequence of the Mw 7.5 Noto Peninsula earthquake likely reflects the effects of the complex fault network, possibly under fluid-rich conditions. The presence of crustal fluid may have played a key role in triggering the initial stage of this earthquake (E1) and the main bilateral rupture process (E3 and E4). The complex fault geometry beneath this area likely contributed to the observed variations in frequency-dependent behavior between E3 and E4, indicating the influence of the fault geometry on the slip and rupture processes during this earthquake.

5. Conclusions

In this study, we performed multi-frequency P-wave back-projection to investigate the frequency-dependent source radiation process of the Mw 7.5 Noto Peninsula earthquake sequence on January 1st, 2024 (comprising the M_{jma} 5.9 and M_{jma} 7.6 events). Our main findings on the complex rupture and radiation processes are summarized as follows:

1. The main source radiation process lasted approximately 44 s, which can be divided into four episodes (E1–E4).
2. *Episode 1 (E1, 0–15 s):* P-wave radiation initiated from the hypocenter, with strong high-frequency energy preceding the lower-frequency

radiation, both concentrated near the hypocentral region.

3. *Episode 2 (E2, 15–30 s):* This stage bridges E1 and the subsequent bilateral rupture, featuring the most intense high-frequency P-wave radiation from the hypocentral area. This stage likely represents the initial growth for the main bilateral rupture stage in the Mw 7.5 earthquake sequence.
4. *Episodes 3 and 4 (E3 and E4):* These stages encompass the main rupture process, propagating bilaterally from the hypocentral region toward the southwestern inland and northeastern offshore areas. The rupture during E4 appears to terminate abruptly at the northeastern fault patch, accompanied by high-frequency emissions at the end of E4.
5. During E3, the low-frequency P-wave radiation dominates, suggesting a relatively long rise time associated with main rupture propagation toward the southwestern inland region.
6. In E4, the frequency content of P-wave radiation initially transitions smoothly from low to high frequencies, then reverses to a high-to-low frequency in the latter half, likely influenced by the complex fault geometry in the northeastern offshore region.

6. Acknowledgments

We thank the editor, Hans Thybo, and two anonymous reviewers for their thoughtful and constructive comments that were helpful in improving the original manuscript. All seismograms used in this study were downloaded from the IRIS Data Management Center (https://ds.iris.edu/ds/nodes/dmc/). This study was partly supported by JST SPRING grant number JPMJSP2119 and JSPS KAKENHI grand number 24KJ0294 to KT. We used ObsPy (Beyreuther et al., 2010) for seismic waveform analysis and data acquisition. To generate all the figures, we used matplotlib (Hunter, 2007), cartopy (Met Office, 2010), Generic Mapping Tools (Wessel et al., 2019), and PyGMT (Uieda et al., 2021). In this study, we employed earthquake catalogs by Global CMT (Ekström et al., 2012) and Japan Meteorological Agency (JMA, 2024a). In Figures 1 and 3, we used the JSPJ fault model (MEXT, 2021).

7. Data Availability

All the seismograms used in this study are available from the IRIS Data Management Center (https://ds.iris.edu/ds/nodes/dmc/).

References

Adda-Bedia, M., Madariaga, R., 2008. Seismic Radiation from a Kink on an Antiplane FaultSeismic Radiation from a Kink on an Antiplane Fault. Bulletin of the Seismological Society of America 98, 2291–2302. doi:10.1785/0120080003.

Amezawa, Y., Hiramatsu, Y., Miyakawa, A., Imanishi, K., Otsubo, M., 2023. Long-Living Earthquake Swarm and Intermittent Seismicity in the Northeastern Tip of the Noto Peninsula, Japan. Geophysical Research Letters 50. doi:10.1029/2022gl102670.

Aoi, S., Asano, Y., Kunugi, T., Kimura, T., Uehira, K., Takahashi, N., Ueda, H., Shiomi, K., Matsumoto, T., Fujiwara, H., 2020. MOWLAS: NIED observation network for earthquake, tsunami and volcano. Earth, Planets and Space 72, 126. doi:10.1186/s40623-020-01250-x.

Beresnev, I.A., 2017. Factors controlling high-frequency radiation from extended ruptures. Journal of Seismology 21, 1277–1284. doi:10.1007/s10950-017-9660-6.

Bernard, P., Madariaga, R., 1984. High-frequency seismic radiation from a buried circular fault. Geophysical Journal of the Royal Astronomical Society 78, 1–17. doi:10.1111/j.1365-246x.1984.tb06468.x.

Beyreuther, M., Barsch, R., Krischer, L., Megies, T., Behr, Y., Wassermann, J., 2010. ObsPy: A Python Toolbox for Seismology. Seismological Research Letters 81, 530–533. doi:10.1785/gssrl.81.3.530.

Bruhat, L., Fang, Z., Dunham, E.M., 2016. Rupture complexity and the supershear transition on rough faults. Journal of Geophysical Research: Solid Earth 121, 210–224. doi:10.1002/2015jb012512.

Ekström, G., Nettles, M., Dziewoński, A., 2012. The global CMT project 2004–2010: Centroid-moment tensors for 13,017 earthquakes. Physics of the Earth and Planetary Interiors 200, 1–9. doi:10.1016/j.pepi.2012.04.002.

FDMA, 2024. Information on Noto Peninsula Earthquake. URL: https://www.fdma.go.jp/disaster/info/2024/.

Fujii, Y., Satake, K., 2024. Slip distribution of the 2024 Noto Peninsula earthquake (MJMA 7.6) estimated from tsunami waveforms and GNSS data. Earth, Planets and Space 76, 44. doi:10.1186/s40623-024-01991-z.

Fukahata, Y., Yagi, Y., Rivera, L., 2014. Theoretical relationship between back-projection imaging and classical linear inverse solutions. Geophysical Journal International 196, 552–559. doi:10.1093/gji/ggt392.

Gabuchian, V., Rosakis, A.J., Bhat, H.S., Madariaga, R., Kanamori, H., 2017. Experimental evidence that thrust earthquake ruptures might open faults. Nature 545, 336–339. doi:10.1038/nature22045.

Hao, J., Ji, C., Yao, Z., 2017. Slip history of the 2016 Mw 7.0 Kumamoto earthquake: Intraplate rupture in complex tectonic environment. Geophysical Research Letters 44, 743–750. doi:10.1002/2016gl071543.

Honda, R., Aoi, S., Matsubara, M., 2024. Characteristics of the source process of the 2024 M7.6 Noto Peninsula earthquake revealed from array back-projection analysis in both low- and high-frequency bands doi:10.21203/rs.3.rs-5732575/v1.

Honda, R., Yukutake, Y., Ito, H., Harada, M., Aketagawa, T., Yoshida, A., Sakai, S., Nakagawa, S., Hirata, N., Obara, K., Kimura, H., 2011. A complex rupture image of the 2011 off the Pacific coast of Tohoku Earthquake revealed by the MeSO-net. Earth, Planets and Space 63, 583–588. doi:10.5047/eps.2011.05.034.

Hunter, J.D., 2007. Matplotlib: A 2D Graphics Environment. Computing in Science & Engineering 9, 90–95. doi:10.1109/mcse.2007.55.

Ishii, M., Shearer, P.M., Houston, H., Vidale, J.E., 2007. Teleseismic P wave imaging of the 26 December 2004 Sumatra-Andaman and 28 March 2005 Sumatra earthquake ruptures using the Hi-net array. Journal of Geophysical Research: Solid Earth (1978–2012) 112. doi:10.1029/2006jb004700.

Ji, C., Archuleta, R.J., Twardzik, C., 2015. Rupture history of 2014 Mw 6.0 South Napa earthquake inferred from near-fault strong motion data and its impact to the practice of ground strong motion prediction. Geophysical Research Letters 42, 2149–2156. doi:10.1002/2015gl063335.

JMA, 2024a. JMA Earthquake Catalog. URL: https://www.data.jma.go.jp/eqev/data/sourceprocess/index.html.

JMA, 2024b. The Seismological Bulletin of Japan. URL: https://www.data.jma.go.jp/svd/eqev/data/bulletin/catalog/notes_e.html.

Kennett, B.L.N., Engdahl, E.R., Buland, R., 1995. Constraints on seismic velocities in the Earth from traveltimes. Geophysical Journal International 122, 108–124. doi:10.1111/j.1365-246x.1995.tb03540.x.

Kind, R., Yuan, X., 2011. Seismic, Receiver Function Technique, Springer Netherlands, Dordrecht, pp. 1258–1269. URL: https://doi.org/10.1007/978-90-481-8702-7_12, doi:10.1007/978-90-481-8702-7_12.

Kiser, E., Ishii, M., 2013. The 2010 Maule, Chile, Coseismic Gap and Its Relationship to the 25 March 2012 Mw 7.1 Earthquake. Bulletin of the Seismological Society of America 103, 1148–1153. doi:10.1785/0120120209.

Kiser, E., Ishii, M., 2016. Back-Projection Imaging of Earthquakes. Annual Review of Earth and Planetary Sciences 45, 1–29. doi:10.1146/annurev-earth-063016-015801.

Koper, K.D., Hutko, A.R., Lay, T., Ammon, C.J., Kanamori, H., 2011. Frequency-dependent rupture process of the 2011 Mw 9.0 Tohoku Earthquake: Comparison of short-period P wave backprojection images and broadband seismic rupture models. Earth, Planets and Space 63, 16. doi:10.5047/eps.2011.05.026.

Kutschera, F., Jia, Z., Oryan, B., Wong, J.W.C., Fan, W., Gabriel, A., 2024. The Multi-Segment Complexity of the 2024 MW ${M}_{W}$ 7.5 Noto Peninsula Earthquake Governs Tsunami Generation. Geophysical Research Letters 51. doi:10.1029/2024gl109790.

Liu, C., Bai, Y., Lay, T., He, P., Wen, Y., Wei, X., Xiong, N., Xiong, X., 2024. Shallow crustal rupture in a major MW 7.5 earthquake above a deep crustal seismic swarm along the Noto Peninsula in western Japan. Earth and Planetary Science Letters 648, 119107. doi:10.1016/j.epsl.2024.119107.

Ma, Z., Zeng, H., Luo, H., Liu, Z., Jiang, Y., Aoki, Y., Wang, W., Itoh, Y., Lyu, M., Cui, Y., Yun, S.H., Hill, E.M., Wei, S., 2024. Slow rupture in a fluid-rich fault zone initiated the 2024 Mw 7.5 Noto earthquake. Science , eado5143doi:10.1126/science.ado5143.

Madariaga, R., 1977. High-frequency radiation from crack (stress drop) models of earthquake faulting. Geophysical Journal of the Royal Astronomical Society 51, 625–651. doi:10.1111/j.1365-246x.1977.tb04211.x.

Madariaga, R., 1983. High frequency radiation from dynamic earthquake fault models. Annales de Geophysique 1, 17–23. URL: http://inis.iaea.org/search/search.aspx?orig_q=RN:14783441.

Madariaga, R., 2003. Radiation from a Finite Reverse Fault in a Half Space. pure and applied geophysics 160, 555–577. doi:10.1007/pl00012550.

Madden, E.H., Ulrich, T., Gabriel, A., 2022. The State of Pore Fluid Pressure and 3-D Megathrust Earthquake Dynamics. Journal of Geophysical Research: Solid Earth 127. doi:10.1029/2021jb023382.

Mai, P.M., Aspiotis, T., Aquib, T.A., Cano, E.V., Castro-Cruz, D., Espindola-Carmona, A., Li, B., Li, X., Liu, J., Matrau, R., Nobile, A., Palgunadi, K.H., Ribot, M., Parisi, L., Suhendi, C., Tang, Y., Yalcin, B., Avşar, U., Klinger, Y., Jónsson, S., 2023. The Destructive Earthquake Doublet of 6 February 2023 in South-Central Türkiye and Northwestern Syria: Initial Observations and Analyses. The Seismic Record 3, 105–115. doi:10.1785/0320230007.

Marguin, V., Simpson, G., 2023. Influence of Fluids on Earthquakes Based on Numerical Modeling. Journal of Geophysical Research: Solid Earth 128. doi:10.1029/2022jb025132.

Marty, S., Passelègue, F.X., Aubry, J., Bhat, H.S., Schubnel, A., Madariaga, R., 2019. Origin of High-Frequency Radiation During Laboratory Earthquakes. Geophysical Research Letters 46, 3755–3763. doi:10.1029/2018gl080519, arXiv:1901.01219.

Matsubara, M., Ishiyama, T., No, T., Uehira, K., Mochizuki, M., Kanazawa, T., Takahashi, N., Kamiya, S., 2022. Seismic velocity structure along the Sea of Japan with large events derived from seismic tomography for whole Japanese Islands including reflection survey data and NIED MOWLAS Hi-net and S-net data. Earth, Planets and Space 74, 171. doi:10.1186/s40623-022-01724-0.

Met Office, 2010. Cartopy: a cartographic python library with a Matplotlib interface URL: https://scitools.org.uk/cartopy.

MEXT, 2021. Annual progress reports of the integrated research project on seis- mic and tsunami hazards around the Japan Sea (FY2019). URL: https://www.eri.u-tokyo.ac.jp/project/Japan_Sea/JSR2Report/index.html.

Mizutani, A., Adriano, B., Mas, E., Koshimura, S., 2024. Fault Model of the 2024 Noto Peninsula Earthquake Based on Aftershock, Tsunami, and GNSS Data doi:10.21203/rs.3.rs-4167995/v1.

Nakajima, J., 2022. Crustal structure beneath earthquake swarm in the Noto peninsula, Japan. Earth, Planets and Space 74, 160. doi:10.1186/s40623-022-01719-x.

Nishimura, T., Hiramatsu, Y., Ohta, Y., 2023. Episodic transient deformation revealed by the analysis of multiple GNSS networks in the Noto Peninsula, central Japan. Scientific Reports 13, 8381. doi:10.1038/s41598-023-35459-z.

Noda, H., Lapusta, N., 2013. Stable creeping fault segments can become destructive as a result of dynamic weakening. Nature 493, 518–521. doi:10.1038/nature11703.

Okuwaki, R., Kasahara, A., Yagi, Y., Hirano, S., Fukahata, Y., 2018. Back-projection to image slip. Geophysical Journal International 216, 1529–1537. doi:10.1093/gji/ggy505.

Okuwaki, R., Yagi, Y., Hirano, S., 2014. Relationship between High-frequency Radiation and Asperity Ruptures, Revealed by Hybrid Back-projection with a Non-planar Fault Model. Scientific Reports 4, 7120. doi:10.1038/srep07120.

Okuwaki, R., Yagi, Y., Murakami, A., Fukahata, Y., 2024. A Multiplex Rupture Sequence Under Complex Fault Network Due To Preceding Earthquake Swarms During the 2024 Mw 7.5 Noto Peninsula, Japan, Earthquake. Geophysical Research Letters 51. doi:10.1029/2024gl109224.

Pampillón, P., Santillán, D., Mosquera, J.C., Cueto-Felgueroso, L., 2023. The role of pore fluids in supershear earthquake ruptures. Scientific Reports 13, 398. doi:10.1038/s41598-022-27159-x.

Rice, J.R., 1992. Chapter 20 Fault Stress States, Pore Pressure Distributions, and the Weakness of the San Andreas Fault. International Geophysics 51, 475–503. doi:10.1016/s0074-6142(08)62835-1.

Rost, S., Thomas, C., 2002. ARRAY SEISMOLOGY: METHODS AND APPLICATIONS: ARRAY SEISMOLOGY. Reviews of Geophysics 40, 2–1–2–27. doi:10.1029/2000rg000100.

Savage, J.C., 1965. The stopping phase on seismograms. Bulletin of the Seismological Society of America 55, 47–58. doi:10.1785/bssa0550010047.

Shinohara, M., Hino, R., Takahashi, T., Obana, K., Kodaira, S., Azuma, R., Yamada, T., Akuhara, T., Yamashita, Y., Kurashimo, E., Murai, Y., lsse, T., Nakahigashi, K., Baba, H., Ohta, Y., Ito, Y., Yakiwara, H., Nakatani, Y., Fujie, G., Sato, T., Shiobara, H., Mochizuki, K., Sakai, S., Ota, Y., Suzuki, S., Isse, T., Abe, H., Hirano, S., Yamahana, H., Sasagawa, Y., Murai, N., Nakao, N., Kaneko, Y., Idoguchi, A., Takahashi, K., Ohta, T., Suzuki, S., Masuda, M., Abe, H., Tanaka, S., Kasaya, T., Ogura, S., Fukushima, S., Hu, C.Y., Yamahana, H., Nakao, N., Fujimura, R., Hirayama, Y., Idoguchi, A., 2025. Precise aftershock activity in the marine source region of the 2024 Noto-Hanto earthquake by rapid response observation using ocean bottom seismometers. Earth, Planets and Space 77, 43. doi:10.1186/s40623-025-02171-3.

Tarumi, K., Yoshizawa, K., 2023. Eruption sequence of the 2022 Hunga Tonga-Hunga Ha'apai explosion from back-projection of teleseismic P waves. Earth and Planetary Science Letters 602, 117966. doi:10.1016/j.epsl.2022.117966.

Tkalčić, H., Chen, Y., Liu, R., Zhibin, H., Sun, L., Chan, W., 2011. Multi-step modelling of teleseismic receiver functions combined with constraints from seismic tomography: crustal structure beneath southeast China. Geophysical Journal International 187, 303–326. doi:10.1111/j.1365-246x.2011.05132.x.

Uieda, L., Tian, D., Leong, W.J., Jones, M., Schlitzer, W., Toney, L., Grund, M., Yao, J., Magen, Y., Materna, K., Newton, T., Anant, A., Ziebarth, M., Wessel, P., Quinn, J., 2021. PyGMT: A Python interface for the Generic Mapping Tools URL: https://doi.org/10.5281/zenodo.5607255, doi:10.5281/zenodo.5607255. the development of PyGMT has been supported by NSF grants OCE-1558403 and EAR-1948603.

USGS, 2024. M 7.5 - 2024 Noto Peninsula, Japan Earthquake. URL: https://earthquake.usgs.gov/earthquakes/eventpage/us6000m0xl/executive.

Vinnik, L., 1977. Detection of waves converted from P to SV in the mantle. Physics of the Earth and Planetary Interiors 15, 39–45. URL: https://www.sciencedirect.com/science/article/pii/0031920177900085, doi:10.1016/0031-9201(77)90008-5.

Wessel, P., Luis, J.F., Uieda, L., Scharroo, R., Wobbe, F., Smith, W.H.F., Tian, D., 2019. The Generic Mapping Tools Version 6. Geochemistry, Geophysics, Geosystems 20, 5556–5564. doi:10.1029/2019gc008515.

Xu, L., Ji, C., Meng, L., Ampuero, J.P., Yunjun, Z., Mohanna, S., Aoki, Y., 2024. Dual-initiation ruptures in the 2024 Noto earthquake encircling a fault asperity at a swarm edge. Science 385, 871–876. doi:10.1126/science.adp0493.

Xu, Y., Koper, K.D., Sufri, O., Zhu, L., Hutko, A.R., 2009. Rupture imaging of the Mw 7.9 12 May 2008 Wenchuan earthquake from back projection of teleseismic P waves. Geochemistry, Geophysics, Geosystems 10, n/a–n/a. doi:10.1029/2008gc002335.

Yagi, Y., Nakao, A., Kasahara, A., 2012. Smooth and rapid slip near the Japan Trench during the 2011 Tohoku-oki earthquake revealed by a hybrid back-projection method. Earth and Planetary Science Letters 355, 94–101. doi:10.1016/j.epsl.2012.08.018.

Yamada, T., Ohta, Y., Nishimura, T., Yoshida, K., Hiramatsu, Y., Kinoshita, Y., 2025. Coseismic slip distribution of the 2024 Noto Peninsula earthquake deduced from dense global navigation satellite system network and interferometric synthetic aperture radar data: effect of assumed dip angle. Earth, Planets and Space 77, 19. doi:10.1186/s40623-025-02154-4.

Yoshida, K., Takagi, R., Fukushima, Y., Ando, R., Ohta, Y., Hiramatsu, Y., 2024. Role of a Hidden Fault in the Early Process of the 2024 Mw7.5 Noto Peninsula Earthquake. Geophysical Research Letters 51. doi:10.1029/2024gl110993.

Yoshida, K., Uchida, N., Matsumoto, Y., Orimo, M., Okada, T., Hirahara, S., Kimura, S., Hino, R., 2023a. Earthquake Data for the 2023 Mw6.2 Suzu Earthquake in the Northeastern Noto Peninsula, Japan URL: https://doi.org/10.5281/zenodo.10019860, doi:10.5281/zenodo.10019860.

Yoshida, K., Uchida, N., Matsumoto, Y., Orimo, M., Okada, T., Hirahara, S., Kimura, S., Hino, R., 2023b. Updip Fluid Flow in the Crust of the Northeastern Noto Peninsula, Japan, Triggered the 2023 Mw 6.2 Suzu Earthquake During Swarm Activity. Geophysical Research Letters 50. doi:10.1029/2023gl106023.

Supplementary Materials for

Frequency-dependent seismic radiation process of the 2024 Noto Peninsula earthquake from teleseismic P-wave back-projection

K. Tarumi[1,*] and K. Yoshizawa[1,2]

[1] Department of Natural History Sciences, Graduate School of Science, Hokkaido University, Sapporo 060-0810, Japan
[2]Department of Earth & Planetary Sciences, Faculty of Science, Hokkaido University, Sapporo 060-0810, Japan.
[*]Corresponding author: tarumi.kotaro.jp@gmail.com

Contents:

- Figures S1–S11.
- Captions of Movie S1.

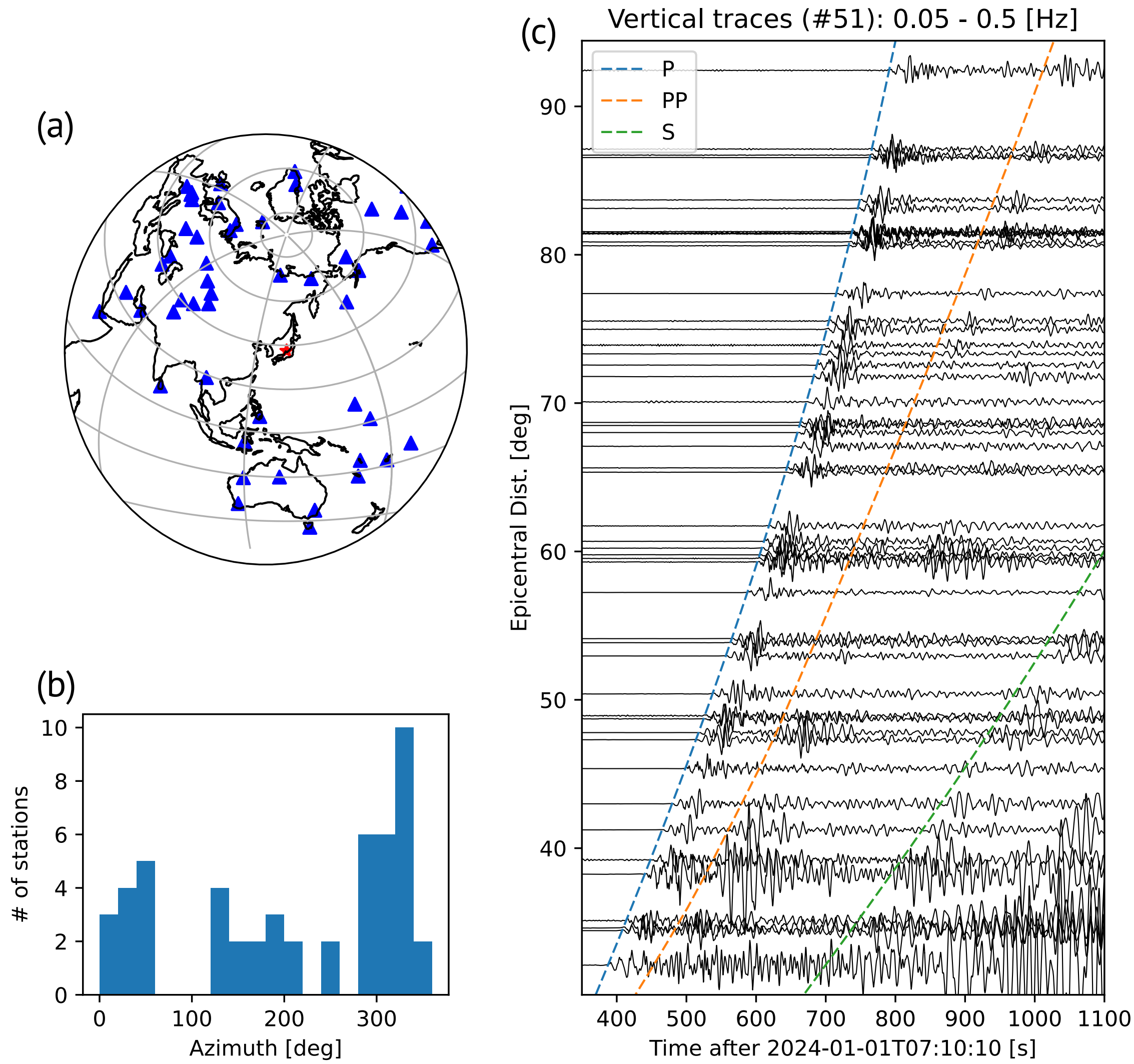

Figure S1. Teleseismic dataset for the frequency range 0.05-0.5 Hz. The figure configuration follows that of Figure 2 in the main text.

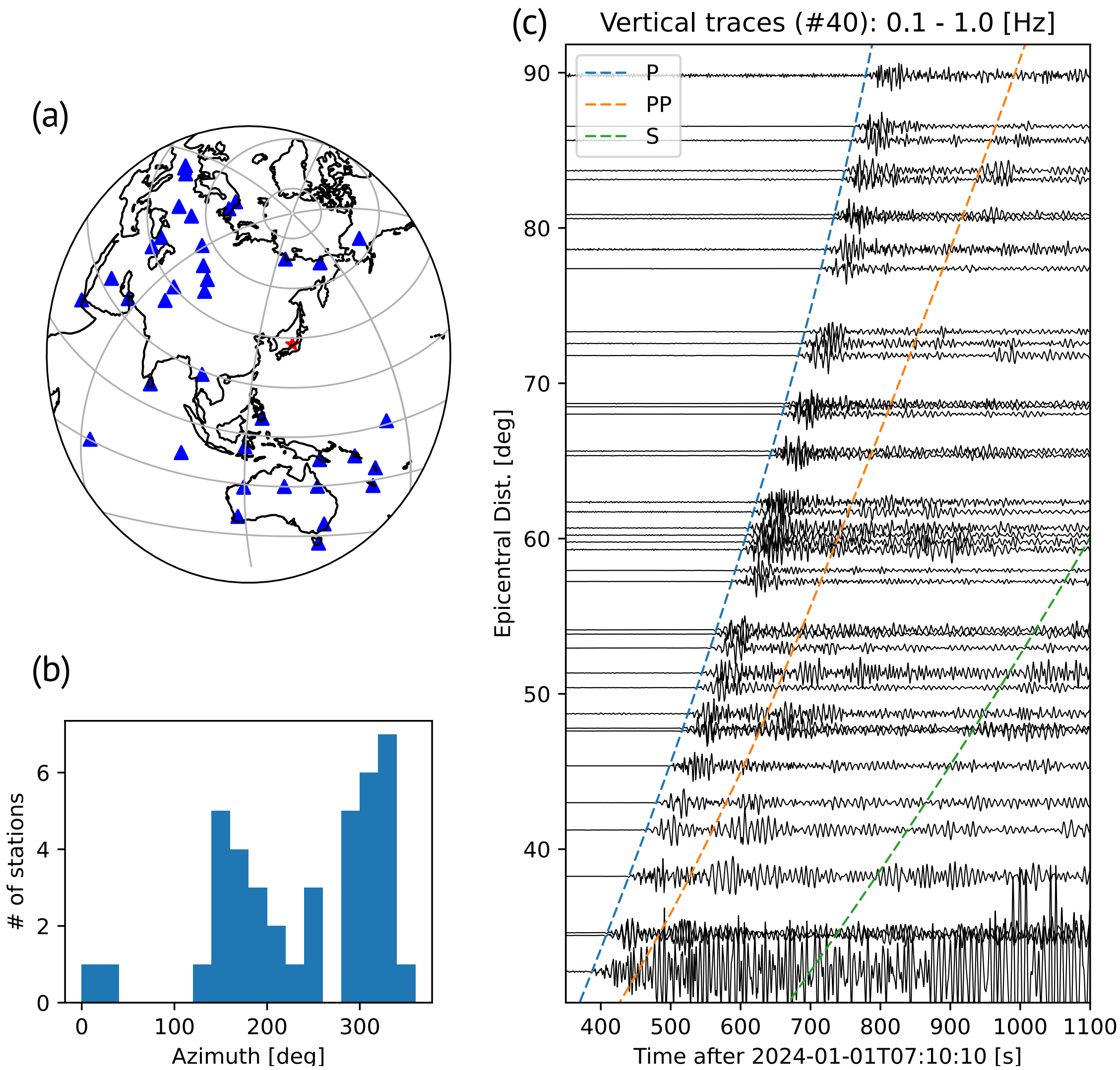

Figure S2: Same as Figure S1, but for 0.1-1.0 Hz.

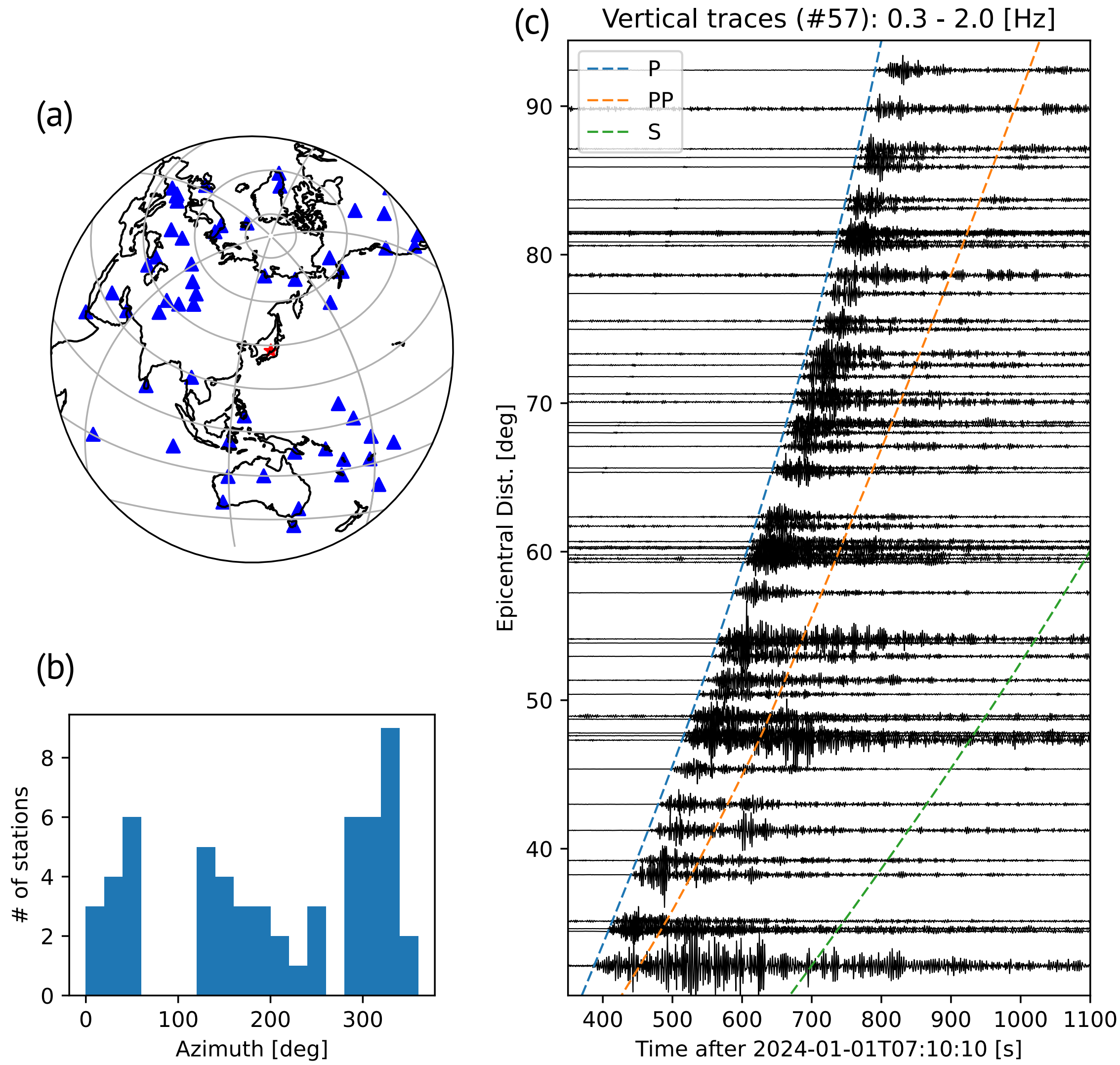

Figure S3: Same as Figure S1, but for 0.3-2.0 Hz.

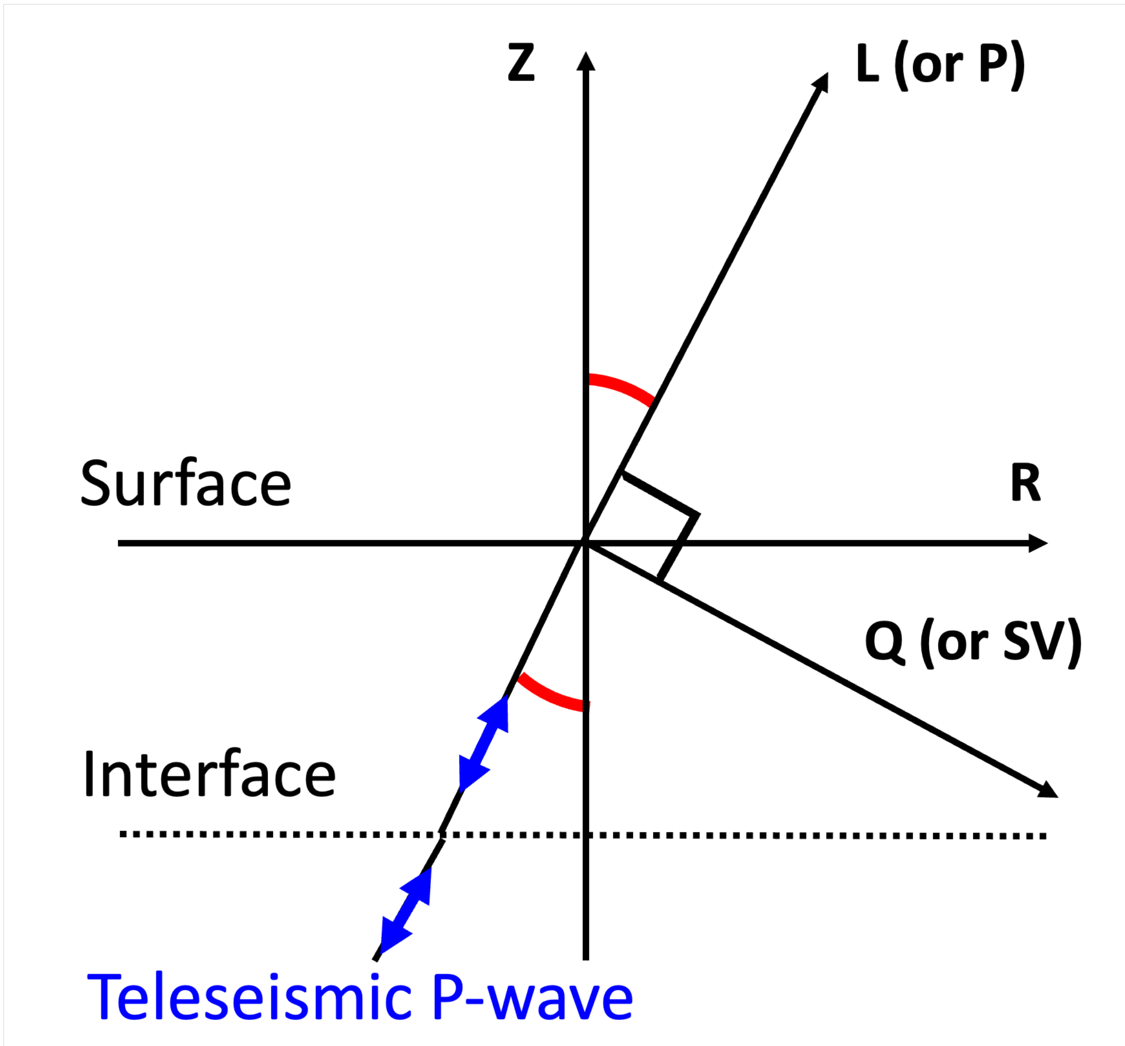

25 Figure S4: Schematic illustration of the LQT coordinate system at a seismic station.

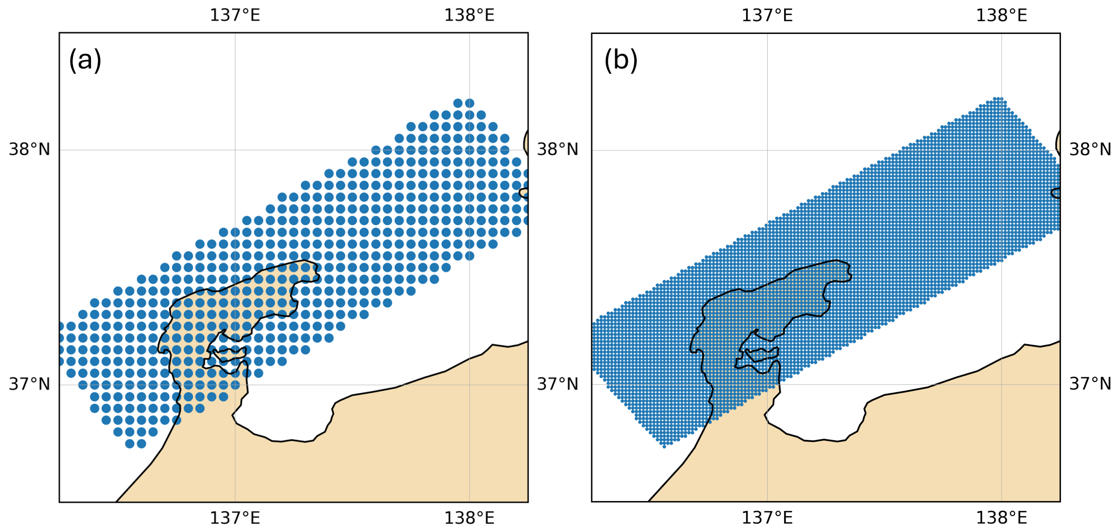

Figure S5: Map view of projected potential source grid points used to generate Figures 5 and S7. (a) 0.05deg girds used for 0.03-0.3, 0.05-0.5, and 0.1-1.0 Hz, (b) 0.015deg used for 0.3-2.0Hz.

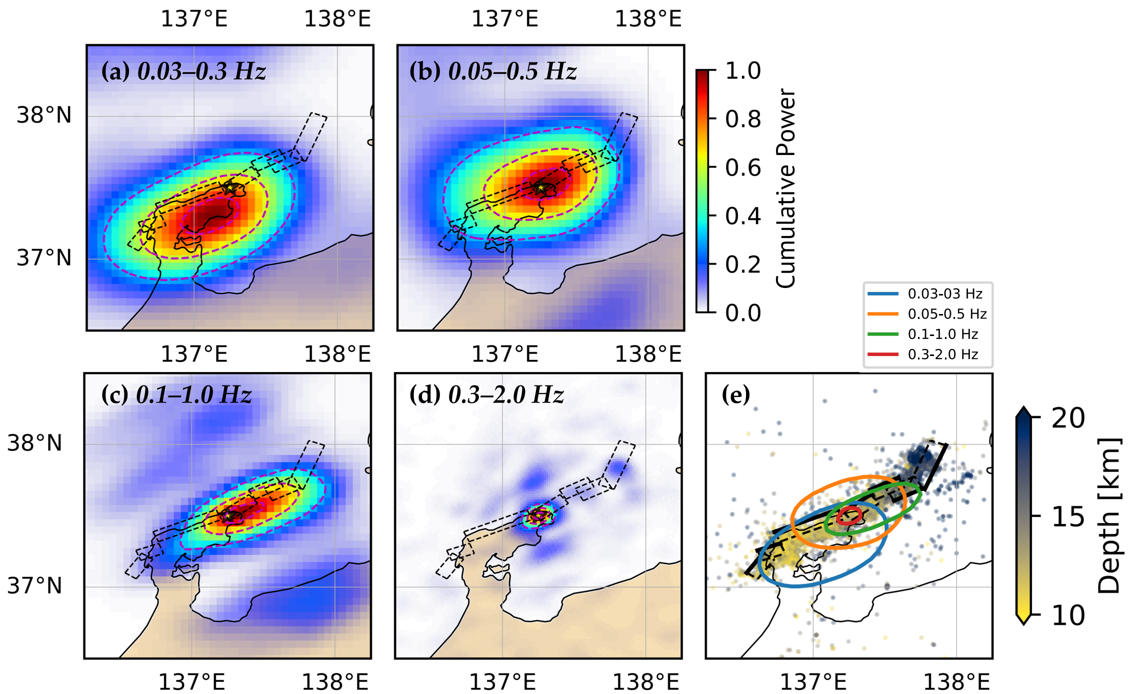

Figure S6: Cumulative radiation power integrated over 44 s for each frequency band: (a) 0.03–0.3 Hz, (b) 0.05–0.5 Hz, (c) 0.1–1.0 Hz, and (d) 0.3–2.0 Hz. (e) Aftershock distributions and the contour lines of 60 % cumulative power.

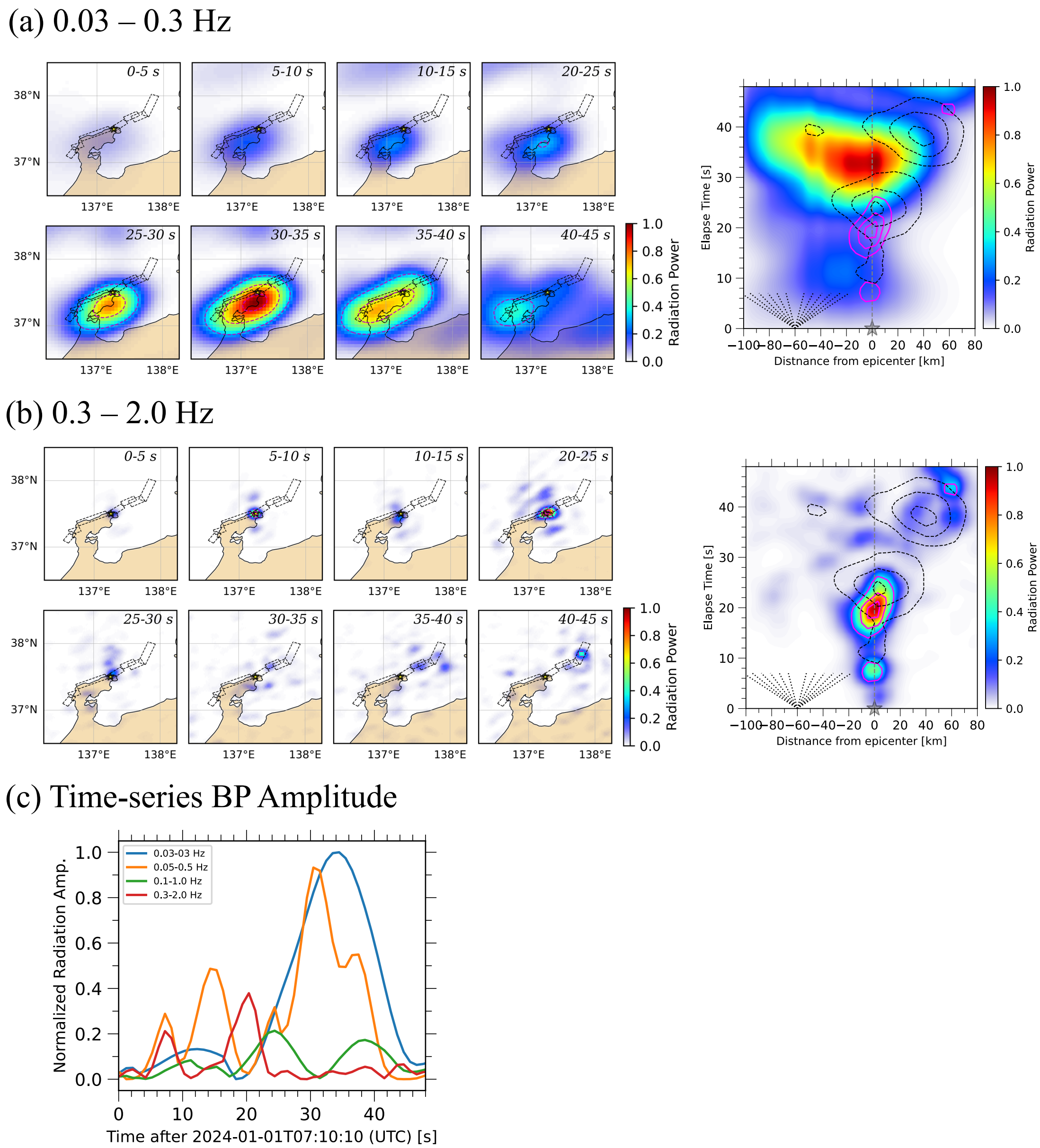

Figure S7: Examples of selected multi-frequency back-projection results using the vertical components without the LQT conversion, following the conventional method using the ZRT coordinate system. (a, b) Snapshots of BP (left panels) and time-dependent P-wave radiation from the source (right panels), projected along N60Eº, as in Figure 3, but using the conventional BP approach. (c) Same as Figure 4, but for the conventional BP method.

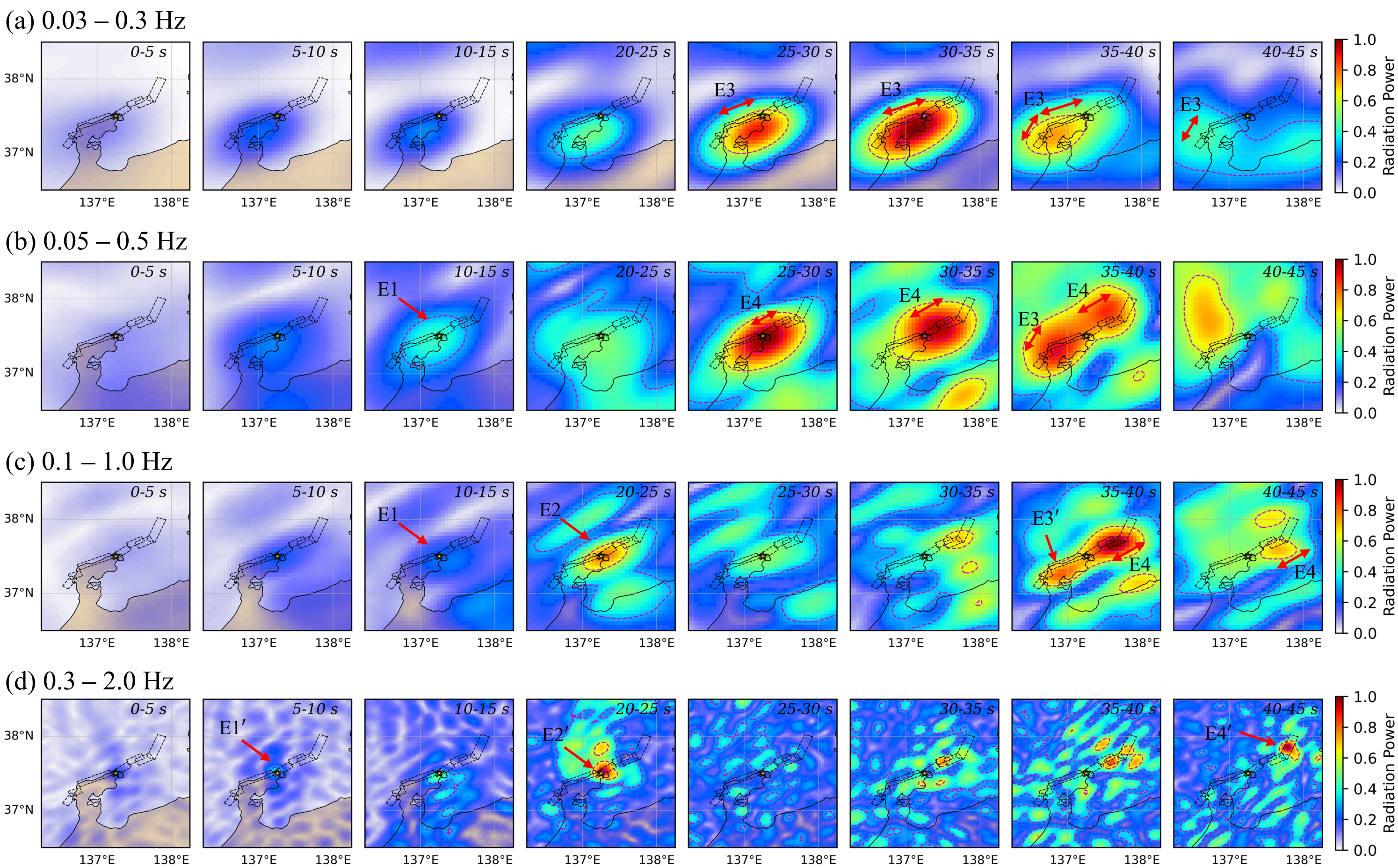

Figure S8: Same as Figure 3, but for the $N = 1$ case in the N-th root stacking process.

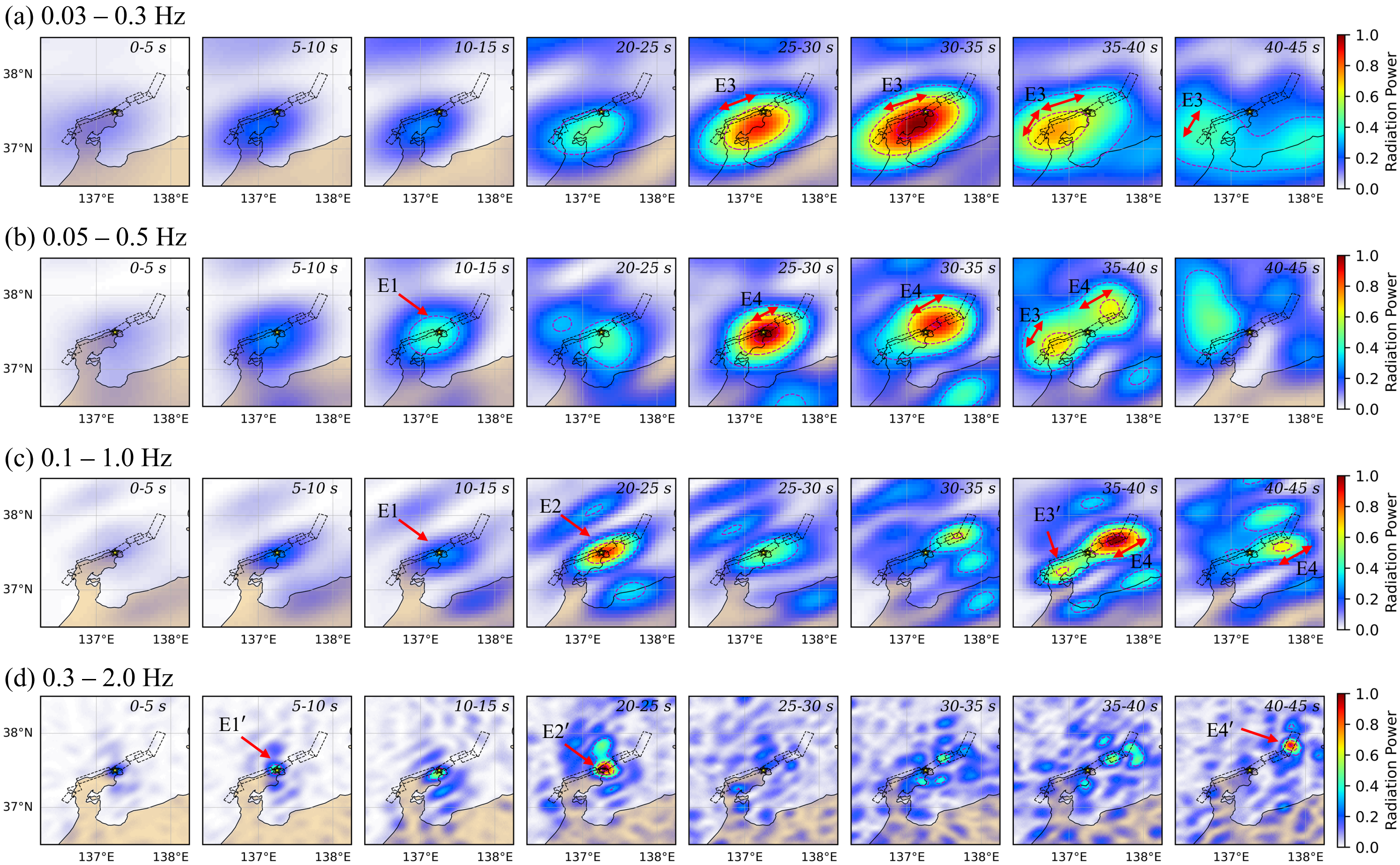

Figure S9: Same as Figure 3, but for the $N = 2$ case in the N-th root stacking process.

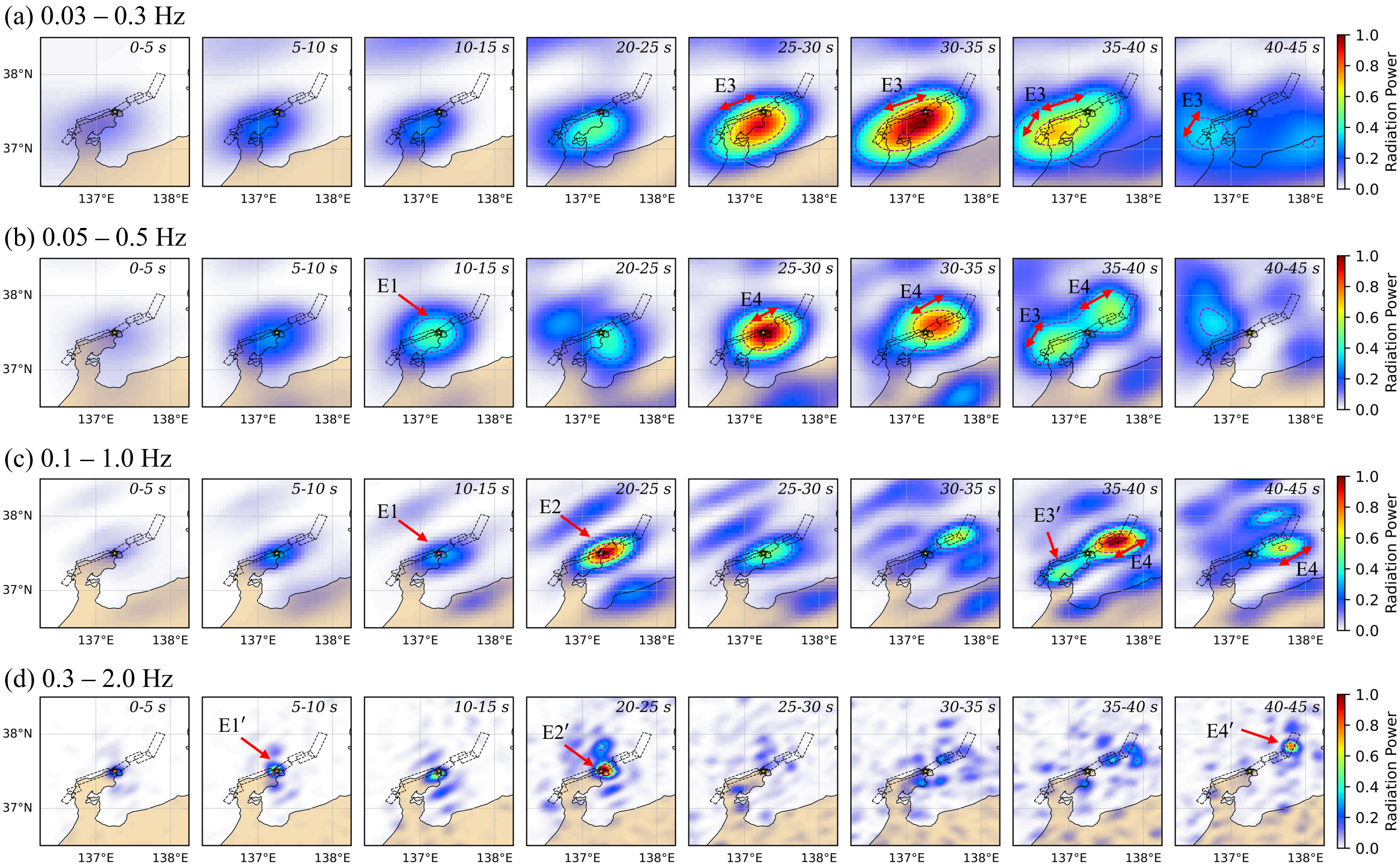

Figure S10: Same as Figure 3, but for the $N = 3$ case in the N-th root stacking process.

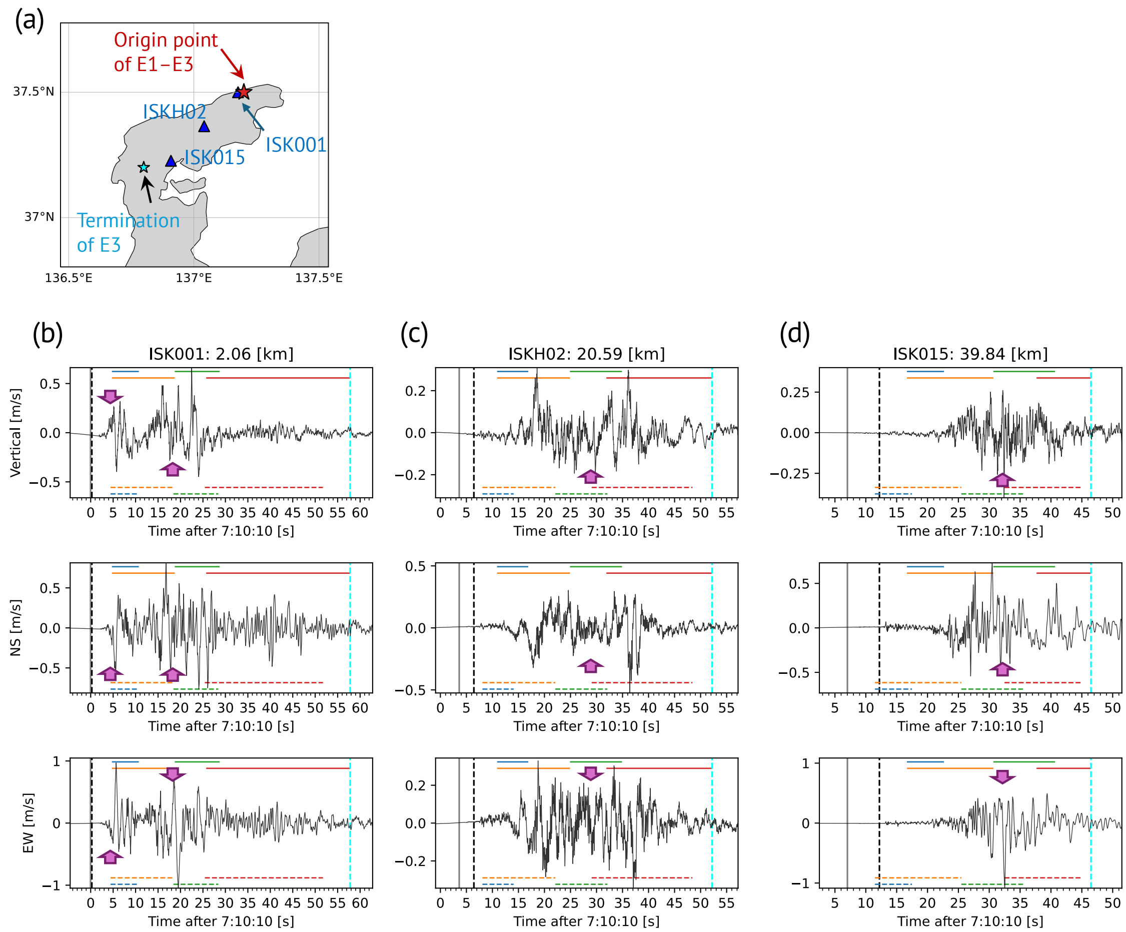

Figure S11: Examples of near-field seismic records at K-NET/KiK-net stations. (a) Map showing stations in the Noto peninsula where the E3 episode is dominant. Red and cyan stars indicate the epicenter of the Mw 7.5 earthquake sequence and the approximate termination point of E3, respectively. Three blue triangles indicate the K-NET/KiK-net stations: ISK001, ISKH02, and ISK015. (b–d) High-pass-filtered (0.03 Hz) velocity waveforms at the three stations. From the top to bottom, vertical, NS, and EW components are shown. Gray solid and black dashed vertical lines indicate the P- and S-wave arrival times from the M_{jma} 5.9 events (7:10:09.54 UTC), while cyan lines show the S-wave arrival times corresponding to the end of E3. Colored dashed and solid horizontal lines represent the duration of P- and S-waves for each inland episode (blue: E1', orange: E1, green: E2, and red: E3). Colored arrows mark the estimated rupture timing beneath each station from our back-projection results, whose colors are the same as those of horizontal lines. Note that two marks (corresponding to E1 and E2) are shown for ISK001, while a single mark (corresponding to E3) is shown for the other two stations.

Movie S1: Snapshots of the P-wave back-projection results: (a) 0.03–0.3 Hz, (b) 0.05–0.5 Hz, (c) 0.1–1.0 Hz, and (d) 0.3–2.0 Hz.